



The ESAFORM benchmark 2023: interlaboratory comparison benchmark for the characterization of microstructural grain growth and dynamic recrystallization kinetics of a single-phase Ni-base superalloy

Julen Agirre¹ · Daniel Bernal¹ · Baptiste Flipon² · Marc Bernacki² · Holger Brüggemann³ · David Bailly³ · Marion Merklein⁴ · Hinnerk Hagenah⁴ · Jan Henning Risse⁴ · Łukasz Madej⁵ · Krzysztof Muszka⁵ · Kamil Cichocki⁵ · Łukasz Poloczek⁶ · Olga Bylya⁷ · Aleksey Reshetov⁷ · Pascal De Micheli⁸ · Julien Barlier⁸ · Andreas Stark⁹ · Uceu F. H. Suhuddin¹⁰ · Peter Staron⁹ · Benjamin Klusemann^{10,11} · Lander Galdos¹

Received: 17 October 2024 / Accepted: 10 March 2025
© The Author(s) 2025

Abstract

This paper presents an extensive benchmark study conducted across eight European research centres, focusing on the high-temperature testing of the Alloy 625 nickel-based superalloy to evaluate its flow behaviour and microstructural evolution, including grain growth (GG) and dynamic recrystallization (DRX). Uniaxial compression tests were performed at 1050 °C and three strain rates (0.1 s⁻¹, 1 s⁻¹, and 10 s⁻¹) using six testing facilities categorised into three types: two conventional thermomechanical machines equipped with electrical resistance furnaces, two deformation dilatometers with induction heating, and two Gleeble machines with Joule heating. Flow curves were compared, and EBSD analysis was conducted to examine DRX. Virtual twins of tests were developed to estimate the thermomechanical history at the centre of the samples, where microstructural observations were conducted. The study methodically discussed the variability in thermomechanical behaviour and DRX results. Additionally, GG was investigated through heat treatments at 1150°C for various hold times, using the three heating methods mentioned. Significant effects of the heating methods on GG were identified. *In-situ* synchrotron analysis at PETRA III DESY provided deeper insights into microstructural evolution. Considering the extensive findings of this research, this paper aims to establish guidelines and define best practices for high-temperature testing to characterise the thermomechanical behaviour and microstructural evolution of materials, while providing insights for advancing experimental mechanics and optimising constitutive model development.

Keywords Benchmark · High temperature testing · Uniaxial compression · Microstructural evolution · Grain growth · Dynamic recrystallization · EBSD analysis · Virtual twins · *In-situ* testing

Introduction

High temperature manufacturing processes such as forging, rolling, and extrusion are essential for shaping metallic materials into functional components used across various industries, including aerospace, automotive, and energy sectors. These processes expose materials to extreme thermal and mechanical conditions, which induce significant microstructural transformations that critically impact the mechanical properties and performance of the final products [1]. The temperature, strain, and strain rate at which

the material is deformed are crucial factors influencing its thermo-mechanical behaviour and the microstructural transformation phenomena during manufacturing processes [2].

Among the key microstructural evolution phenomena observed during high temperature manufacturing processes of single-phase metals are grain growth, dynamic recrystallization (DRX) and post-dynamic recrystallization (PDRX) which includes static (SRX) and meta-dynamic (MDRX) recrystallization regimes [3, 4]. These mechanisms are fundamental to understand and to optimize the process-structure-property relationships [5]. GG refers to the minimization of the total grain boundary (GB) network energy and so, to the increase in average grain size over time at elevated

Extended author information available on the last page of the article

temperatures [6, 7], impacting material strength, ductility, and other mechanical properties. DRX, on the other hand, is the process of nucleation and growth of new grains during deformation due to plastic deformation and dislocations accumulation, resulting in refined grain structures and improved material properties [8]. Furthermore, PDRX phenomena occur after deformation, influencing the final microstructure and properties of the material [9]. Understanding these microstructural evolution mechanisms in high temperature manufacturing processes is essential for optimizing process parameters, enhancing material performance, and ensuring the reliability of manufactured components across various industrial sectors [5].

Alloy 625, also known as Inconel 625, is a face-centred cubic (FCC) single-phase solid-solution strengthened nickel-based superalloy renowned for its exceptional corrosion resistance, high strength at elevated temperatures, and excellent weldability, standing as a cornerstone material in advanced industries, such as aerospace, oil and gas, and energy [10]. However, the utilization of Alloy 625 comes with substantial cost considerations due to its high market value and the complexity of its manufacturing requirements, which arise from its high strength even at elevated temperatures. These challenges are compounded by the demands of high-temperature manufacturing processes, such as forging and rolling, and the possible subsequent heat treatment, which require precise control and optimization of the manufacturing parameters [11]. Ensuring the desired microstructure in this superalloy necessitates accurate definition and fine-tuning of process parameters such as temperature, strain rate, and cooling rates during these high-temperature manufacturing processes. The cost-intensive nature of Alloy 625 underscores the critical importance of minimizing scrap and achieving consistent microstructural properties through precise process control, thus maximizing material utilization and component performance in demanding applications [12–14].

Laboratory-scale thermomechanical testing plays a pivotal role in characterizing and modelling the flow behaviour and microstructural evolution phenomena in materials like Alloy 625, which are essential for defining optimal process parameters [5]. These tests offer a controlled environment to simulate the complex thermomechanical conditions encountered during high-temperature manufacturing processes. By subjecting samples to controlled temperature, strain rate, and deformation conditions, researchers can systematically study the flow behaviour and the microstructural evolution phenomena under diverse process conditions [15–17]. The insights gained from such testing not only aid in understanding fundamental flow and microstructural mechanisms but also contribute to the development of robust predictive models for material behaviour under varying processing conditions [18–22]. Furthermore, any numerical model requires

calibrated experimental data to isolate the physical parameters necessary for its use. Bridging experimental data with computational modelling enhances process designers' ability to optimize manufacturing processes, predict material performance, and design components with tailored microstructures and enhanced mechanical properties [23, 24].

Diverse thermomechanical testing equipment is employed for experimental testing, each utilizing distinct heating methods, drive systems, lubrication methods and cooling systems to simulate different high-temperature manufacturing conditions [5]. Universal tension–compression machines or purpose-built testing facilities equipped with electric furnace offer controlled heating environments suitable for studying microstructural evolution under steady-state conditions [25]. Commercial deformation dilatometers, employing induction heating, enable rapid heating rates, a precise temperature control and fast quenching, making them ideal for investigating DRX phenomena during high temperature deformation processes [26]. Thermo-mechanical deformation machines, such as Gleeble® machines, can also utilize Joule heating coupled with hydraulic or servo-mechanical drive systems to provide advanced capabilities for simulating complex thermomechanical loading conditions encountered in industrial processes like forging and rolling [27]. These three types of laboratory machines encompass the primary testing facilities used today for high-temperature material testing. By leveraging these diverse testing platforms, researchers gain valuable insights into the hardening and microstructural evolution of materials like Alloy 625, contributing to the development of robust process-microstructure-property relationships.

The use of diverse testing facilities with different heating, motion-control and cooling systems can lead to varied experimental results when characterizing the hardening and the microstructural evolution of advanced materials. Very few papers in the literature have systematically assessed the discrepancies arising from the utilization of different testing facilities on the experimental characterization of microstructural transformation phenomena. Nicolay et al. investigated the influence of heating methods on recrystallization (ReX) phenomena in Alloy 718 [28]. The authors examined both SRX and DRX regimes by comparing the effects of Joule heating and conventional heating in a radiative furnace. Remarkably, this study stands out as one of the few to delve into this specific area of research. The findings suggest that the choice of heating method may significantly impact the microstructural evolution of the material under investigation, shedding light on an important yet underexplored aspect of experimental mechanics of materials. With the same objective, Rheinheimer et al. investigated the effect the electrical field could have in the high temperature grain growth evolution of the perovskite oxide strontium titanate [29]. They concluded that the electrical field promotes grain growth, and thus, a higher grain-boundary mobility.

Another factor contributing to differences in results can be attributed to the microstructural observation techniques employed to analyse the resulting microstructure of the tested samples. Limited comparative studies could only be identified on this matter. Flipon et al. conducted a comparative analysis between microstructural results obtained through electron backscatter diffraction (EBSD) analysis and those derived from image analysis based on backscattered electron (BSE) or optical micrographs (OM) [30]. They focused on two materials: an austenitic stainless steel and a hexagonal close-packed zirconium alloy. Additionally, their study examined the influence of data processing parameters on grain size determination. Similarly, Wright conducted a parametric study on EBSD scanning parameters to assess their influence on grain size determination in polycrystalline microstructures [31]. Both studies highlight that the choice of microstructural observation methodology can significantly affect the microstructural characterization results and that terminology is also of prime importance when discussing grain size or recrystallized fraction, as these terms can carry many different mathematical formulations in the literature, despite the existence of ISO or ASTM standards on the subject.

In summary, while the literature provides limited studies in this area, there remains a notable gap within the scientific community: the absence of a benchmark for comparing equivalent tests conducted under identical conditions across different testing facilities, in the field of flow behaviour and microstructural evolution characterization of metallic materials. To address this gap, this research paper undertakes an important initiative. Equivalent thermo-mechanical tests were conducted in six distinct testing facilities and systematically compared, representing a significant step forward in the field. These facilities encompass two universal compression machines equipped with electrical resistance furnaces, two commercial quenching and deformation dilatometers featuring induction heating, and two commercial compression machines employing Joule heating. By meticulously designing and executing systematic procedures, this research aims to contribute to the standardization of experimental protocols and enhance the reliability of results in materials science research.

In this research paper, samples extracted from the same Alloy 625 bar underwent a uniform heat treatment process in a single furnace to homogenize the initial microstructure, ensuring consistency across all samples. Two distinct studies were then conducted. The first focused on analysing the influence of heating methods (conventional radiative furnace, induction, and Joule) on GG behaviour in the absence of deformation. The second involved high-temperature uniaxial compression tests conducted at the six mentioned testing facilities to assess their impact on the flow behaviour and microstructural results. Following the tests, all samples were

subjected to EBSD analysis using identical scanning parameters. Furthermore, in order to mitigate potential variations in EBSD data processing, a standardized post-processing methodology was applied to all EBSD files.

To enhance the precision of this experimental benchmark, precise virtual twins of all testing facilities were developed within the FORGE® simulation software [24]. These virtual twins were generated to accurately represent crucial testing parameters such as the heating method, kinematics and friction conditions in each machine. These simulations were employed to numerically estimate the thermomechanical history of the central region of the samples, where microstructural observations were conducted.

To complement the performed analyses, investigations were carried out at the PETRA III storage ring at the Deutsches Elektronen-Synchrotron (DESY) facility, where *in-situ* measurements of microstructural evolution were acquired during high-temperature GG heat treatments and uniaxial compression tests. This complex experimental setup allowed for real-time observation of microstructural changes as the samples underwent thermal processing and mechanical deformation, providing valuable insights into the dynamic behaviour of materials at complex high-temperature conditions.

Considering the extensive findings of the research, the objective of this paper was to establish guidelines, standardize methodologies, and define best practices for conducting experimental tests aimed at characterizing the hardening and microstructural evolution phenomena of materials at high temperatures. It is important to highlight that the goal of this research paper was not to favour or criticize any specific testing facility or machine, but rather to objectively assess differences that may arise from employing different testing equipment.

Hereunder, the research centres and companies that participated in this ESAFORM benchmark study are presented (Table 1):

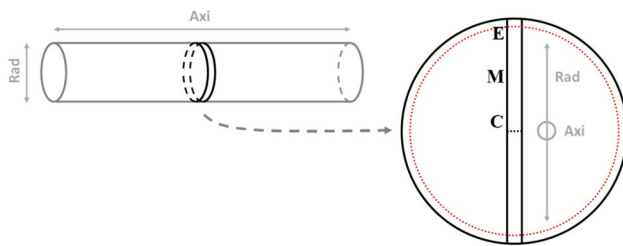
Material and experimental procedure

Selected material: Alloy 625

The samples employed in this study for the experimental tests were cut by wire electrical discharge machining (EDM) from the circumferential edge of a Ø160mmx1800mm hot forged and unannealed Alloy 625 bar provided by the producer of high-performance materials VDM Metals GmbH (Fig. 1). The Alloy 625 nickel-based superalloy was selected due to its characteristics as an austenitic single-phase FCC material with no phase change, making it an ideal candidate for the current investigation.

Table 1 Participating partners in the ESAFORM 2023 benchmark project, performed tests and testing facilities employed per partner

Partner	Abbreviation	Tests	Facility
CEMEF Mines Paris PSL	CEM	GG and DRX	Conventional compression machine with radiative furnace
University of Strathclyde—Advanced Forming Research Centre	AFRC	DRX	
Mondragon Unibertsitatea	MU	GG and DRX	TA Instruments DIL805 A/D/T compression dilatometer with induction heating
RWTH Aachen University – Institute of Metal Forming	IBF	DRX	
AGH University of Krakow in cooperation with Lukasiewicz – GIT	AGH/L-GIT	GG and DRX	Gleeble 3800 with Joule heating
FAU Erlangen-Nürnberg – Institute of Manufacturing Technology	LFT	DRX	Gleeble 3500 with Joule heating
Helmholtz-Zentrum Hereon GmbH	HER	GG and DRX	TA Instruments DIL805 A/D/T compression dilatometer in PETRA III DESY synchrotron
Transvalor	TSV	Virtual twins	FORGE® simulation software

**Fig. 1** Identification (in dashed red circle) of the circumferential edge from which the samples for this study were cut. E=circumferential edge of the bar; M=mid-radius; C=centre

It is important to note that the same Alloy 625 raw material was used for all the tests performed in all the research centres, to rule out any influence that the difference in chemical composition and/or the initial microstructure could have on the performance of the material during the tests. The chemical composition of the employed Alloy 625 is presented in Table 2.

The initial microstructure of the Alloy 625 Ø160 mm bar varied from its centre to the edge. The equiaxed microstructures in the centre (C), mid-radius (M) and edge (E) of the initial bar are illustrated in Fig. 2 (a, c and e, respectively), clearly showing a finer microstructure in the circumferential edge of the circular section. The mean grain size was measured with light microscopy (LM) following the circular intercept method of the ASTM-E112-12 standard [32]. The mean grain size in ASTM was converted to microns by interpolating the Table 4 of the ASTM-E112-12 standard. Mean grain sizes resulted to be 17.0 µm (8.8 ASTM) in the centre, 15.9 µm (9.0

ASTM) in the mid-radius, and 7.7 µm (11.1 ASTM) at the edge of the initial bar.

Optical microscopy observations are complemented by kernel average misorientation (KAM) maps (Fig. 2 (b, d and e)) obtained by EBSD data post-treatment. The KAM parameter provides an insight of the amount and spatial distribution of stored energy (evaluated thanks to the dislocation density) and is defined as the orientation difference between one pixel and its neighbouring pixels. It is a local value, each pixel of the image has a discrete KAM value, and it is calculated as:

$$\text{KAM}(i) = \frac{1}{n} \sum_{j=1}^n \theta_{ij}, \quad (1)$$

where n is the number of neighbouring pixels of i , and θ_{ij} is the disorientation between pixels i and j . Neighbours can be limited to only 1st level neighbouring pixels, but can also be increased to more surrounding pixel-levels [33].

Before distributing the samples to the partners participating in the benchmark, the samples underwent a homogenization heat treatment for 30 min at 1,150°C in an electrical furnace (Hobersal CRN-5X/17 PAD P) at MU. According to the literature, the solvus temperature of Alloy 625 is 1,060°C [34]. Figure 3 depicts the KAM maps of the as-received material at the circumferential edge, and after the pre-test solution annealing of 30 min at 1,150°C. The differences in grain size and misorientation angle before and after the heat treatment can be clearly seen. As expected, after the solution annealing, the grain size increases, and a reduction in dislocation density is evident, with a final grain size of 86.4 µm at the circumferential edge.

Table 2 Chemical composition of the employed Alloy 625 [wt. %]

Ni	Cr	Mo	Fe	Nb	Ti	Al	Si	Mn	C	P	S
59.6	22.3	9.1	4.6	3.4	0.33	0.23	0.15	0.05	0.02	0.006	0.001

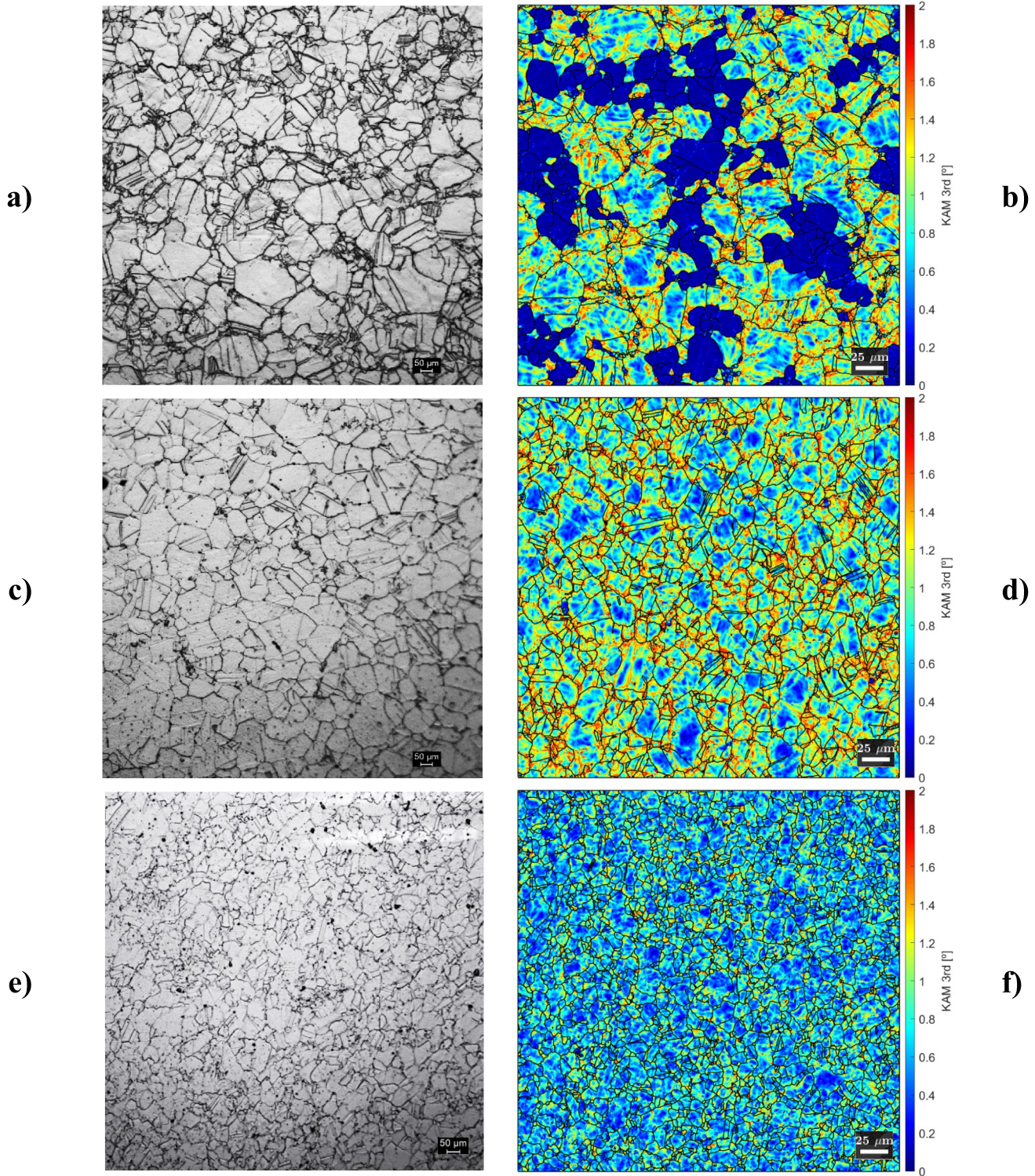


Fig. 2 LM micrographs of initial alloy 625 bar at the **a**) centre (C), **c**) mid-radius (M), and **e**) edge (E). KAM maps at the **b**) centre, **d**) mid-radius, and **f**) edge

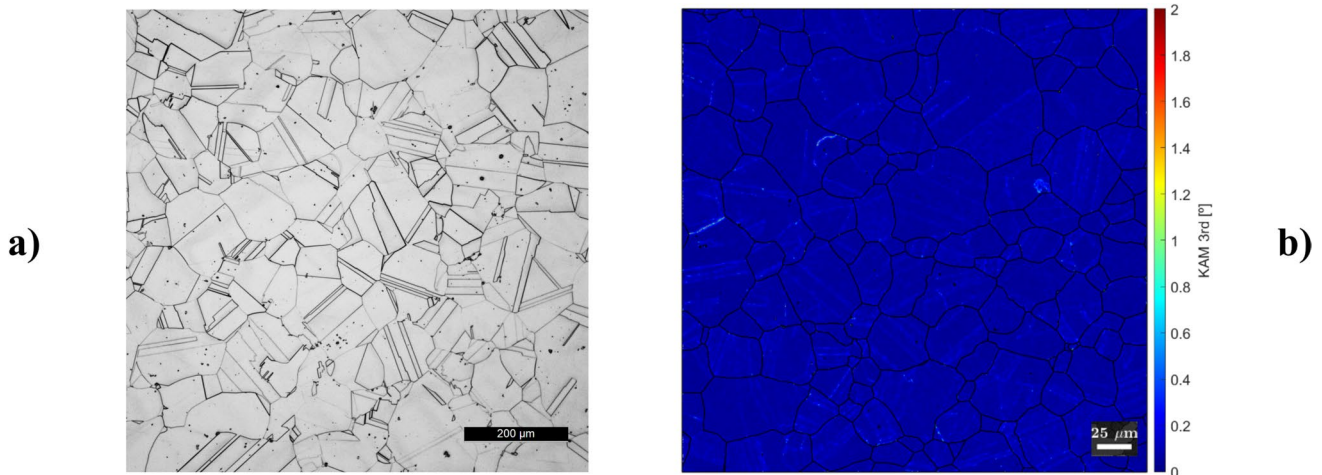
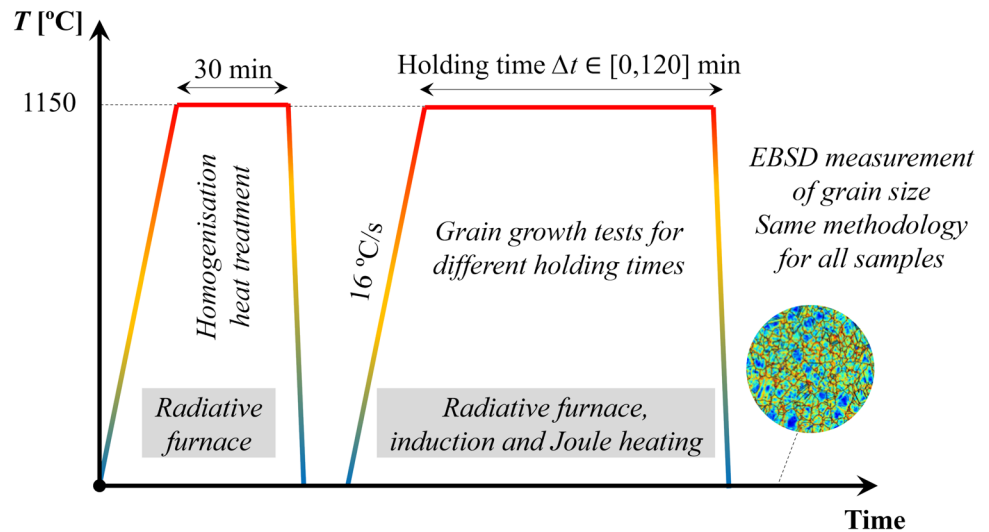


Fig. 3 a) LM micrograph and b) KAM map of the microstructure at the circumferential edge after a solution annealing of 30 min at 1,150°C

Fig. 4 Experimental procedure applied to cylindrical specimens to assess the influence of the heating technology on grain growth kinetics



GG tests

The GG testing procedure as illustrated in Fig. 4, was applied to the cylindrical samples using three machines and heating technologies.

Samples were tested in conventional electrical furnaces preheated to 1150°C at CEMEF and MU. Ø10mm×L15mm samples were used in the tests, and the heating rate was monitored using thermocouples, which resulted in an average heating rate of 16°C/s. After reaching the objective temperature, a heat treatment at 1150°C for a duration $\Delta t \in [0; 120]$ minutes was applied to the sample to study the GG kinetics of the material.

With the objective to study the influence of the heating technology on the GG kinetics, the same procedure

was repeated using Joule effect heating in a Gleeble 3800 machine at AGH//L-GIT and using induction heating in a TA Instruments DIL 805A/D/T dilatometer at MU. In order to mimic the same heating profile as the one recorded in the conventional electrical furnaces at CEMEF and MU, a heating rate of 16°C/s was defined in both machines. The standard sample sizes of Ø10mm×L12mm and Ø5mm×L10mm were used for the Gleeble and the dilatometer tests, respectively.

All samples were quenched in a maximum of 2 s at the end of the holding time to freeze the microstructure. To compare the samples and the resulting microstructure, all the samples were prepared for microstructural analysis following the procedure explained in "[Metallographic preparation and microstructural analysis](#)" section.

Compression tests to study the thermomechanical behaviour and DRX kinetics

To assess the influence of the heating technology on DRX kinetics, hot compression tests were performed in the same thermomechanical conditions on six different devices, which are classified and schematized by machine type in Fig. 5. As detailed in "Selected material: Alloy 625" section, all cylindrical samples underwent a homogenization heat treatment at 1,150°C for 30 min in an electrical furnace at MU prior to the uniaxial compression tests. This ensured a consistent initial material state across all cases. The sample diameters and heights varied among testing facilities, as illustrated in Fig. 5, and were determined based on the maximum force capacity of each testing machine.

Two conventional tension/compression machines equipped with a furnace were used for the thermomechanical testing of samples using conventional electrical heating. Two Gleeble machines (3800 and 3500) were used for the thermomechanical testing of samples using Joule effect heating. Finally, two TA Instruments DIL 805 A/D/T dilatometers were employed to test the samples using induction heating.

Based on previous work [35] with the same Alloy 625 material, macroscopic strains were defined for each machine and testing condition (strain rate and fixed temperature). The ultimate goal of all tests was to achieve an approximate 50% recrystallized fraction at each strain rate and testing facility.

To accomplish this, numerical modelling of the process was performed using the approach described in "Virtual twin of experimental tests" section, along with a thermomechanical and a Johnson–Mehl–Avrami–Kolmogorov (JMAK) ReX model developed by Agirre et al. at MU [35]. In the initial simulations, a Tresca shear friction factor of $m = 0.4$ was assumed, and facility-dependent sample geometries were used. The resulting macroscopic strains to be reached at each testing condition and facility are summarized in Table 3.

The testing procedure for the thermo-mechanical compression tests is illustrated in Fig. 6, and the specific details used at each facility are provided below:

- **CEMEF:** MTS Landmark 370–25 (hydraulic) machine equipped with a conventional LGTEC electrical radiative furnace. Samples were introduced to the furnace and held in the testing position for 5 min to reach the testing temperature. Temperature control was performed using the thermocouple of the furnace, and two K-type thermocouples were located at the ends of the two tools (TC1 and TC2) to monitor the local temperature near the sample, as shown in Fig. 5(a). Sample dimensions were $\text{Ø}10\text{mm} \times \text{L}15\text{mm}$. All the samples were water-quenched just after testing to freeze the microstructure. Boron nitride was used as a lubricant.
- **AFRC:** Zwick/Roell Z150 (Screw driven test frame, $\dot{\epsilon} = [< spanclass = 'convertEndash' > 0.01 - 0.1 < /span >] \text{s}^{-1}$)

Fig. 5 Graphical representation of the employed testing facilities

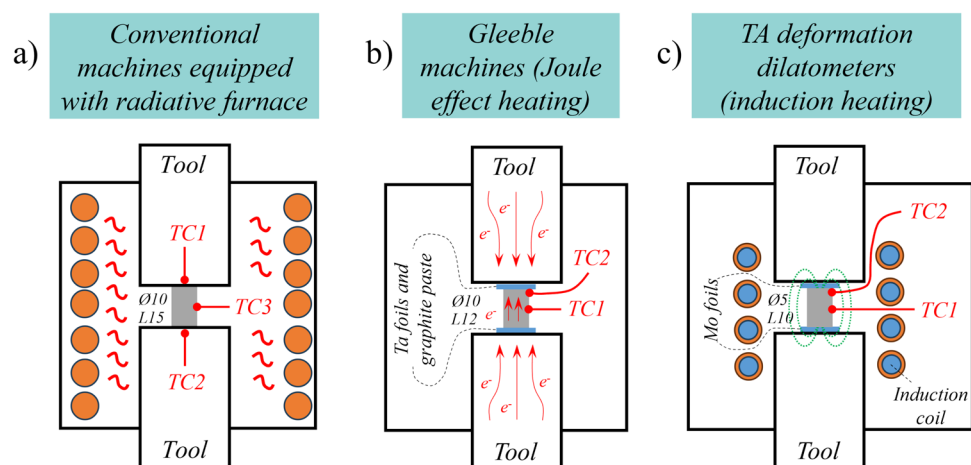
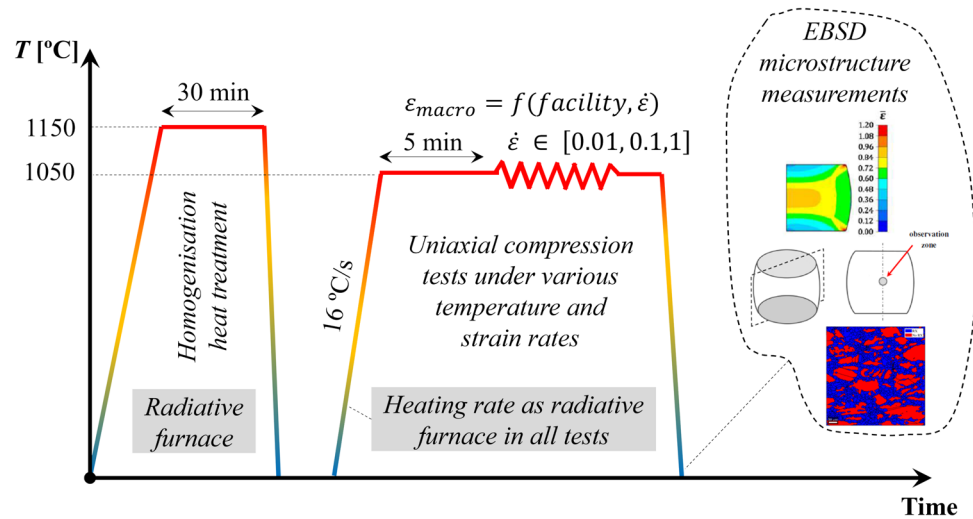


Table 3 Macroscopic strains (ϵ) used in the compression tests for the different testing facilities and strain rates ($\dot{\epsilon}$). *tests in LFT were not performed with constant true strain rate but at constant speed

Testing facility	True strain rate [s^{-1}]		
	$\dot{\epsilon}=0.01$	$\dot{\epsilon}=0.1$	$\dot{\epsilon}=1.0$
Conventional machines with electric furnace (CEMEF and AFRC)	$\epsilon = 0.53$	$\epsilon = 0.62$	$\epsilon = 0.69$
TA Instruments DIL 805A/D/T (MU, IBF and HER)	$\epsilon = 0.6$	$\epsilon = 0.68$	$\epsilon = 0.75$
Gleeble 3800 and 3500 machines (AGH/L-GIT and LFT*)	$\epsilon = 0.54$	$\epsilon = 0.65$	$\epsilon = 0.74$

Fig. 6 Experimental procedure of uniaxial compression tests for hardening and DRX analysis



and Zwick/Roell Amsler HA250 (Hydraulic, $\dot{\epsilon} = 1\text{s}^{-1}$) equipped with a conventional electrical radiative furnace. Samples were introduced to the furnace at room temperature. Then both the furnace and the sample were heated together to the testing temperature in 1 h. Temperature control was performed using one K-type thermocouple located at the centre of the sample (TC3) as shown in Fig. 5(a). Sample dimensions were $\text{Ø}10\text{mm} \times \text{L}15\text{mm}$. Boron nitride was employed as lubrication, and samples were water-quenched just after testing to freeze the microstructure.

- **AGH/L-GIT and LFT:** Gleeble 3800 and 3500 machines (Joule effect heating). Temperature control was performed using a central K-type thermocouple (TC1), and an additional K-type thermocouple was located in one of the sample ends to monitor the thermal gradient within the sample (TC2), as shown in Fig. 5(b). Tantalum foils and graphite paste were used as lubricants and to reduce the thermal gradient between the sample and anvils. Sample dimensions were $\text{Ø}10\text{mm} \times \text{L}12\text{mm}$. Samples were water-quenched just after testing to freeze the microstructure.
- **MU and IBF:** TA Instruments DIL 805A/D/T dilatometers (induction heating). Temperature control was

performed using a central S-type thermocouple (TC1), and an additional S-type thermocouple was located in one of the sample ends to monitor the thermal gradient within the sample (TC2), as shown in Fig. 5(c). Molybdenum foils were used as lubricants and to reduce the thermal gradient between the sample and anvils. Sample dimensions were $\text{Ø}5\text{mm} \times \text{L}10\text{mm}$. Samples were argon quenched just after testing to freeze the microstructure.

It is important to highlight that all uniaxial compression tests, except those conducted at LFT, were performed with a constant macroscopic true strain rate ($v(t)/h(t)$). In most studies found in the literature, which investigate flow behaviour and DRX phenomena, tests are carried out at a constant macroscopic true strain rate [36, 37]. To analyse the impact of maintaining a constant true strain rate versus a constant speed (variable true strain rate) on both the flow curves and the DRX kinetics, the LFT tests were performed at a constant speed. This methodological choice was made to specifically isolate and examine the effects of strain rate consistency. The findings from this analysis are detailed later in "In-situ GG results" section.

Since the quenching time following the completion of the uniaxial compression test significantly influences the DRX kinetics results [15], Table 4 summarizes the

Table 4 Post-deformation cooling times in the uniaxial compression tests for the analysis of DRX kinetics

Partner	Facility	Post-deformation cooling time [s]
CEM	Conventional compression machine with radiative furnace	1.18—1.8
AFRC		15
MU	TA Instruments DIL805 A/D/T compression dilatometer with	2
IBF	induction heating	2
AGH/L-GIT	Gleeble 3800 with Joule heating	1
LFT	Gleeble 3500 with Joule heating	1

post-deformation cooling times for all research centres. Quenching times are below 2 s in all the cases, except the samples tested at AFRC, which had longer cooling times (15 s).

As in the previous grain growth tests, for the comparison of the samples and the resulting microstructure, all the samples were prepared for microstructural analysis following the procedure explained in "Metallographic preparation and microstructural analysis" Section.

***In-situ* GG and DRX tests at DESY synchrotron**

A dilatometer DIL 805A/D/T from TA instruments was used for *in-situ* testing at hutch EH3, operated by Hereon, of beamline P07 at the PETRA III storage ring at Deutsches Elektronen-Synchrotron (DESY) shown in Fig. 7. Unlike in the previous tests, and to analyse the homogenisation step *in-situ*, the samples were not homogenised previously. Thus, all phases were conducted within the *in-situ* testing facility. This included homogenisation (30 min/1150 °C, heating rate 16 K/s), quenching (cooling rate 100 K/s), holding at room temperature for 5 min, followed by subsequent heating and deformation phase, and the final quenching.

The samples had a size of Ø5 mm × L10 mm, and 100 µm Mo foils were inserted at both ends to reduce the temperature gradient between stamps and sample. The temperature was controlled by a type S thermocouple spot welded on the sample, as depicted in Fig. 5c. The processing chamber was flooded with He to 800 mbar before the test. X-rays with a photon energy of 103 keV and a beam cross-section of 400 µm × 400 µm were used to record images with a set of full diffraction rings using a PerkinElmer area detector with a pixel size of 200 µm at a distance of 1.362 m from the sample. Exposure times were between 0.1 and 2 s. As in the

DRX tests, three different strain rates were used (0.01 s⁻¹, 0.1 s⁻¹ and 1 s⁻¹).

Diffraction rings are only homogeneously filled with intensity when the grain size of the material is sufficiently small. As the grain size increases, the rings become increasingly spotty; single large spots originate from single large grains. It is worth mentioning that this effect also depends on the cross-section of the X-ray beam—a larger beam includes more diffracting grains. Although there is no standard method to derive a mean grain size from this effect, qualitative conclusions can be drawn. For this purpose, FIT2D [38, 39] was used to produce tables with intensity along a diffraction ring, integrated in the radial direction over the peak width. These tables were used to calculate the roughness of a diffraction ring. The roughness of a diffraction ring is defined as:

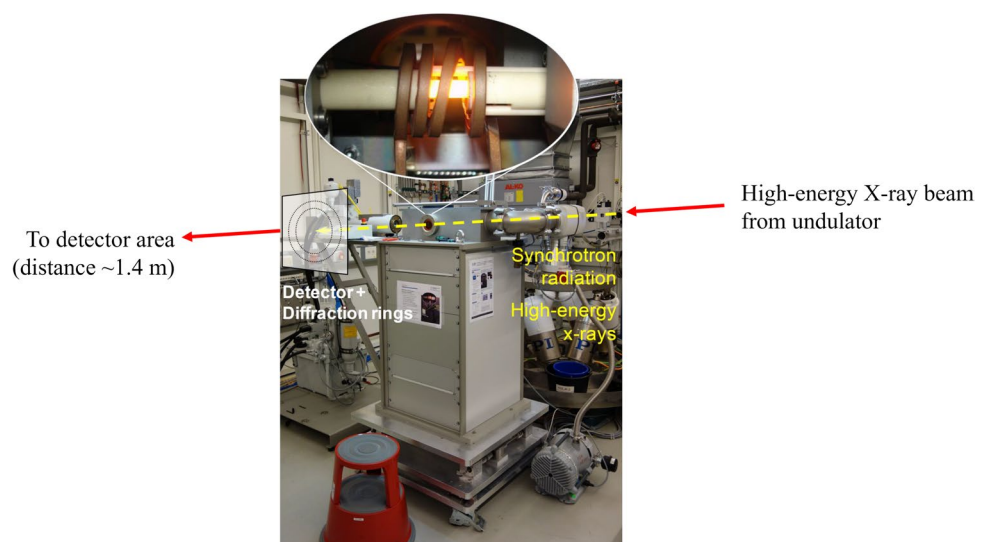
$$R = \frac{1}{\bar{I}} \sqrt{\frac{1}{n-1} \sum_{i=2}^n (I_i - \bar{I})^2}$$

where I_i is the intensity along the diffraction ring from 0 to 360°, n is 3600 and \bar{I} is the mean value of the intensity along the ring. R describes the root mean square of intensity differences between neighbouring segments on the diffraction ring. Similar approaches have been used before [40]. The calculation method used here does not add roughness to an intensity plateau on the diffraction ring, unlike calculations based on the difference from a mean value.

Virtual twin of experimental tests

The test configuration for the compression tests must be carried out with meticulous methodology, as many factors influence the final result. Although high strain and strain

Fig. 7 TA instruments DIL 805A/D/T dilatometer at hutch EH3 of beamline P07 at the PETRA III storage ring at the deutsches elektronen-synchrotron (DESY)



rates are achievable with compression mode testing, there are inherent difficulties that affect the quality of the results, even if the experimental setup is carefully defined and executed. The main drawbacks during high-temperature compression testing are friction between the anvils and the temperature inhomogeneity. The latter is primarily caused by heat transfer between the sample and the tools and the adiabatic heating of the sample, which is more pronounced at high testing speeds. Friction can be minimized but never completely avoided by using appropriate lubrication and contact foils, which serve as a lubricant, and reduce the heat transfer coefficient between the anvils and the testing sample. On the other hand, the adiabatic heating of the sample is practically uncontrollable. During high-temperature and high-speed testing, heating occurs in a short time, making in-line temperature control using welded thermocouples nearly impossible.

As a consequence, neither the strain rate nor the temperature remains constant during the test. The best way to handle these effects and account for them when extracting the test results is to measure them as accurately as possible during the test. The temperature at the outer edge of the sample can be recorded by thermocouples, and this temperature is expected to be very similar to that at the centre of the sample given the small size of the samples. However, deviations may occur longitudinally if the insulation between the tools and sample is not effectively performed, resulting in an inhomogeneous testing temperature. Similarly, the macroscopic strain can be measured using high-temperature extensometers or pushing rods that follow the tool during deformation. However, if barrelling occurs due to friction, the strain and strain rate at the centre of the sample can differ significantly from the calculated macroscopic strain.

For these reasons, developing a relatively simple yet accurate virtual twin through numerical simulation is crucial

to indirectly estimate the real centre thermo-mechanical conditions (temperature, strain, and strain rate) by using the experimentally measured signals (temperature and kinematics). This is particularly important because the centre of the sample is typically used for microstructural evaluation after the test. Various numerical models were developed by Transvalor in the FORGE® simulation software during the benchmark to inversely calculate the thermo-mechanical conditions at the sample centre. A local constitutive model for Alloy 625, developed by Agirre et al. at MU, was employed for the simulations [35].

Although current technology allows for the simulation of Joule heating and induction heating, as demonstrated in [41, 42], determining the specific features of the heating sources remains challenging and unknown to researchers. Experimentally, it is known that there is a longitudinal thermal gradient in the TA dilatometers and Gleeble machines although using tantalum and molybdenum foils for insulation purposes ("[Thermomechanical characterisation](#)" section). Taking advantage of this information, three models were developed, see Fig. 8.

The first model, the simplest, assumes no temperature loss between the sample and the tools or surrounding air, and no adiabatic heating of the samples is taken into account (Fig. 8a). This is considered a simple and accurate approximation since the induction heaters and Joule heating devices continuously control the temperature to keep it as constant as possible. Additionally, the entire setup is heated to the testing temperature in the electrical oven, making this model well-suited for such cases.

To validate this approach, two additional numerical models were developed. In the second model (Fig. 8b), adiabatic heating of the sample is considered, and a high heat transfer coefficient ($HTC = 20,000 \text{ W/m}^2\text{K}$) between the sample and the ambient temperature is included, with the ambient

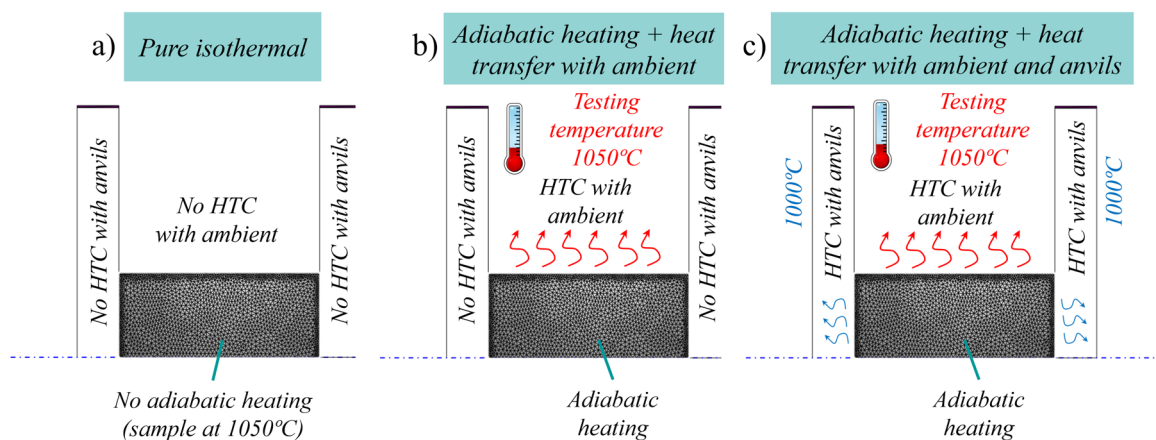


Fig. 8 Simplified numerical models created to simulate the high temperature compression tests: **a)** Isothermal case with no adiabatic heating; **b)** Adiabatic heating case with heat transfer with ambient; **c)** Full model considering adiabatic heating and heat transfer with anvils and ambient

temperature set to the testing temperature in the simulation. The goal of this model is to capture the continuous heating action of the machines and to study the radial and longitudinal thermal gradients in the sample due to adiabatic heating. The heat transfer with the ambient air ensures that the sample cools down to the surrounding ambient temperature, even when adiabatic heating occurs. This feature may be important for slow velocity tests, where, without heat transfer, the sample's temperature would increase during testing.

Finally, the third model (Fig. 8c) incorporates adiabatic heating, heat transfer with the ambient temperature, as well as heat transfer (HTC = 20,000 W/m²K) with the tools, which are maintained at 1000°C, 50°C lower than the sample testing temperature. This model takes into account longitudinal thermal gradients that may arise during heating and compression due to cooling through the anvils, as well as thermal loss or gain with the ambient temperature, set to match the testing temperature. This model permits the study of the effects of radial and longitudinal thermal inhomogeneities on strain rate and strain calculations at the centre of the sample, which is the primary aim of the models. The employed HTC values are extremely high, and the model is used to estimate the error that the isothermal model might produce in the worst-case scenario.

All the models were created using the FORGE® software, with the sample dimensions matching those used in the Gleeble machines (Ø10mm × L12mm). This sample size was chosen because it has the potential for the largest radial thermal gradients simply due to its larger radius. Firstly, the effect of friction on the local strain rate and strain in the sample centre was evaluated. This parameter significantly influences barrelling and the disparity between the macroscopic and centre strain rate and strain, and it is crucial for researchers to set it accurately to obtain precise thermomechanical conditions occurring in the sample centre. For this purpose, three different friction values were employed, ranging from sliding ($m=0$) to moderate friction ($m=0.4$), using the Tresca shear friction model.

Simulations were conducted utilizing the isothermal numerical model outlined in Fig. 8a. As depicted in Fig. 9, the friction coefficient notably affects the strain and strain rate in the sample centre. The strain rate is not constant and differs from the macroscopic constant strain rates defined in the simulation, which utilizes a non-constant anvil displacement ($\Delta h = h_0 [1 - \exp(\dot{\epsilon}t)]$). As observed, the strain rate is close to the theoretical nominal strain rate when a frictionless situation is simulated. As friction increases, barrelling also increases, which enhances the inhomogeneity of the strain field. In these cases, the strain rate exhibits a hyperbolic shape, increasing at the beginning and then showing a decreasing trend as the test progresses. The equivalent strain distributions across the samples' cross-sections at the final macroscopic strain state are also presented in the graphs.

Figure 10 shows the effect of heat transfer on the centre strain. In all cases the friction factor was set as $m=0.4$. In the isothermal model (Fig. 8a) and the model that accounts for adiabatic heating and heat transfer with the ambient (Fig. 8b), the results are identical. Small differences are also observed in the model that accounts for adiabatic heating, heat transfer with the ambient, and heat transfer with anvils (Fig. 8c). This model aims to demonstrate exaggerated errors due to non-homogeneous sample temperature, primarily caused by the cooling of the samples through contact with the anvils. In this third model the barrelling shape changes with a more pronounced bulging in the sample centre, causing slight deviations in the strain field.

In view of these results, all the centre strains presented in this work hereafter were calculated via the isothermal model. It has been sufficiently demonstrated that the strain field in the sample centre is governed by the barrelling shape, which primarily changes with the friction coefficient. Moreover, the numerical model can be adjusted for each testing setup and condition by only modifying the friction coefficient and using inverse simulation. This approach corrects both

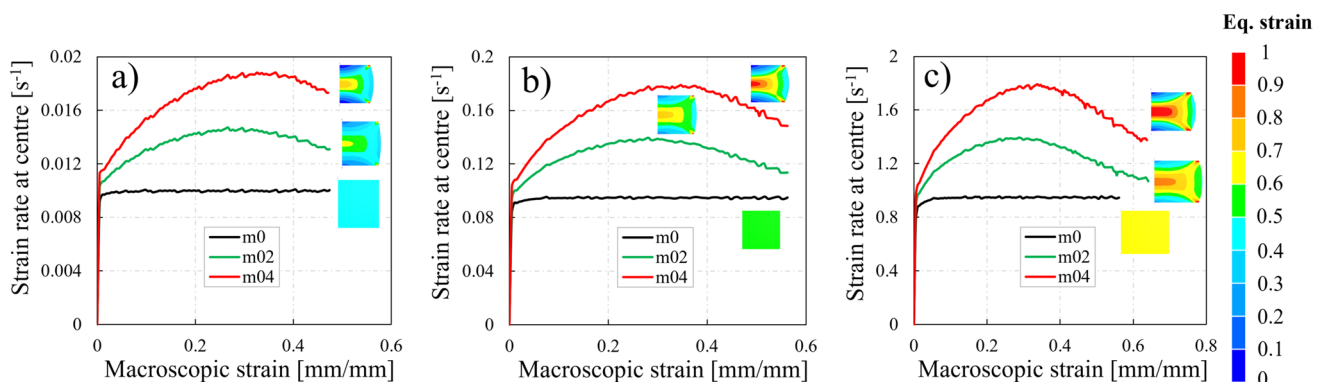


Fig. 9 Effect of friction factor ($m=0$ – 0.4) on strain rate in the sample centre. Macroscopic strain rates of **a)** 0.01 s^{-1} , **b)** 0.1 s^{-1} and **c)** 1 s^{-1}

friction effects and temperature inhomogeneities by adjusting a single parameter and using a simple numerical model that does not account for any heat transfer.

The friction coefficient was adjusted for all the tests performed on the different machines used in this benchmark. The optimization of the friction coefficient was done by considering the final maximum and minimum diameters

measured in the samples after deformation, caused by barrelling (Fig. 11).

The average maximum and minimum diameters observed in the different machines and tests are depicted in Fig. 12, where the experimental and numerical diameters of all the tests together with their standard deviations are shown. In general, the results showed minimal variation among tests

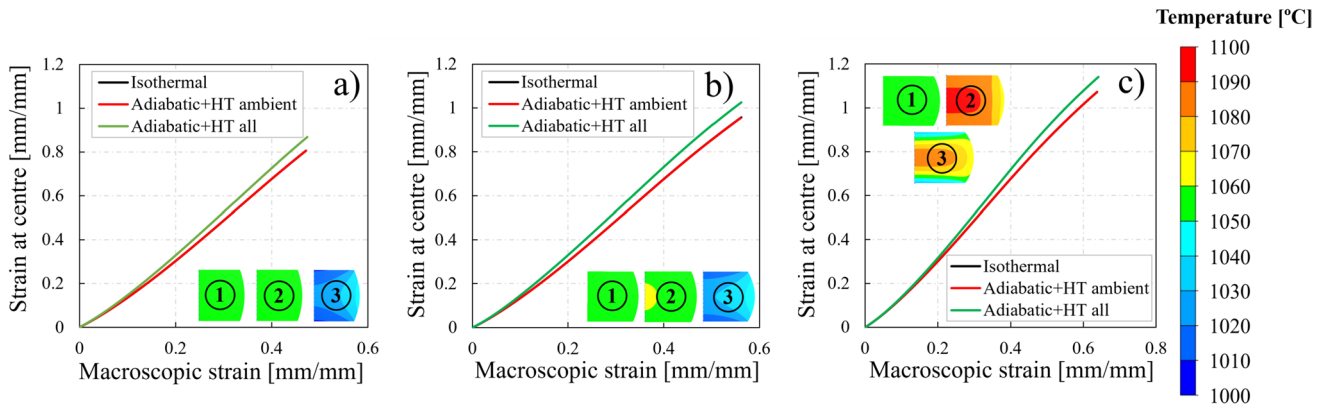


Fig. 10 Influence of the heat transfer on the strain in the sample centre. Macroscopic strain rates of **a)** 0.01 s^{-1} , **b)** 0.1 s^{-1} and **c)** 1 s^{-1} . Employed friction factor in all cases: $m=0.4$. ⓪: Isothermal, ⊙: Adiabatic + HT ambient, ⊚: Adiabatic + HT all

Fig. 11 Experimental barrelling of the samples tested at the different research centres. *Conv.* = Conventional compression machine with radiative furnace | *Dil.* = Compression dilatometer with induction heating | *Gle.* = Gleeble with Joule heating

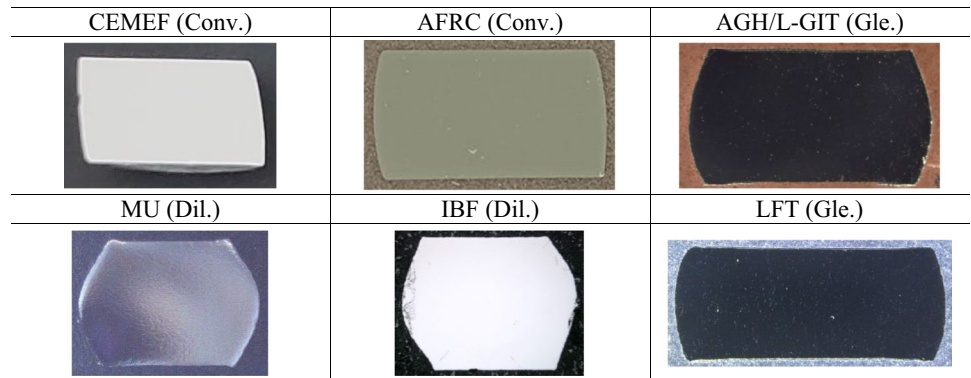
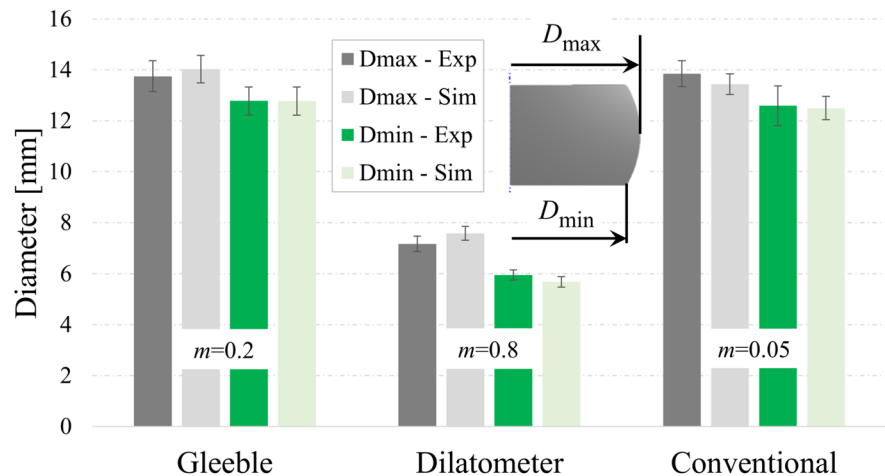


Fig. 12 Experimental and numerical barrelling of tested samples based on the employed testing facility, along with the estimated tresca shear friction factor (m) for each case



conducted on the same type of machine. All the Gleeble tests were tuned using a friction factor of $m=0.2$, which showed a good fit with the experimental results. Similarly, the results obtained with the dilatometers were fitted with a friction coefficient of $m=0.8$. The conventional machines equipped with an electric furnace exhibited the smallest friction, with a friction coefficient of $m=0.05$.

To finish with this section, the evolution of the equivalent strain rate at the sample centre, estimated through inverse simulations, is presented in Fig. 13. The results reveal a direct correlation between the evolution of equivalent strain rate and both the friction between the sample and tools and the kinematics of the testing facility's moving tool (constant vs. non-constant macroscopic strain rate, explained later in "Thermomechanical characterisation" section).

Higher friction, as observed in dilatometers at MU and IBF, results in a more pronounced barrelling effect, leading to a significant increase in equivalent strain rate during compression. Conversely, due to low friction, the equivalent strain rate at the sample centre remains relatively constant in tests conducted at AGH/L-GIT, CEMEF and AFRC.

The impact of tool kinematics, whether maintaining a constant strain rate or constant speed, as explained later in "Thermomechanical characterisation" section, is

evident when comparing the equivalent strain rate evolution between AGH/L-GIT (constant strain rate) and LFT (constant speed). With constant strain rate tool kinematics, the equivalent strain rate remains nearly constant at the centre, whereas with constant speed tool kinematics, the equivalent strain rate gradually increases with strain. Ideally, low friction and constant strain rate are desirable to maintain a constant equivalent strain rate at the centre. If the tests are performed with high friction or constant speed, the equivalent strain rate in the centre significantly increases. However, as the variations in strain rate are relatively minor and do not involve changes in the order of magnitudes, the observed differences are not expected to considerably influence the DRX kinetics.

Metallographic preparation and microstructural analysis

Once all the GG and the DRX tests were performed in all the research centres, the microstructure of the centre of each tested sample was measured with the EBSD technique in different SEMs. To this end, the tested samples were sectioned from the central cutting plane parallel to

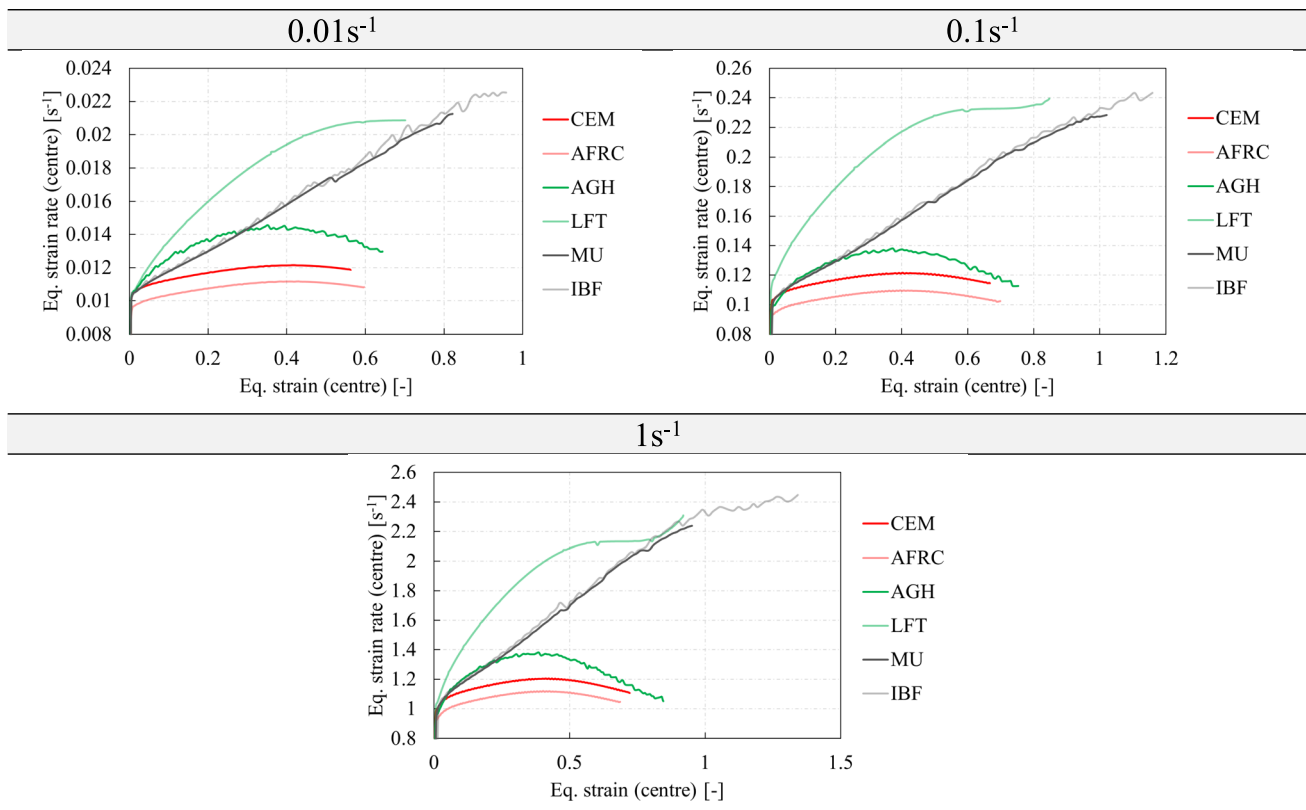


Fig. 13 Equivalent strain rate in the centre of the DRX tested samples estimated by inverse simulation in FORGE® for macroscopic strain rates of 0.01 s^{-1} , 0.1 s^{-1} and 1 s^{-1}

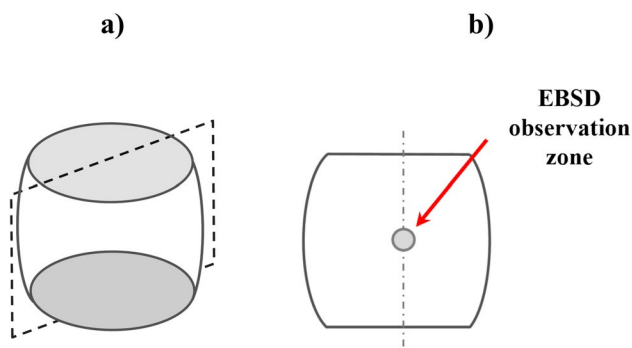


Fig. 14 a) Cutting plane of the cylindrical samples tested to study the DRX evolution of alloy 625, and b) location of EBSD observations in the central zone of the samples

the deformation direction (Fig. 14a), and all samples were prepared for EBSD analysis. The microstructure in the central zone of the samples was analysed (Fig. 14b), as this was the zone with the highest strain localization due to the barrelling effect.

The samples were prepared for the microstructural analysis according to the following methodology:

- **CEMEF:** Sample cutting using a micro-cutting machine with cut-off wheels. Standard metallographic preparation:
 - 1) Sample hot mounting in non-conductive resin (just used for polishing steps).
 - 2) Polishing with SiC papers (from 320 to 4000 grit size).
 - 3) Polishing with diamond solutions 3 μm and 1 μm .
 - 4) Vibratory polishing with colloidal silica for 3 h.
 - 5) Unmounting of the sample from the resin.
- **AFRC:** Samples were cut using a micro-cutting machine and mounted in a conductive resin for EBSD. This was followed with the standard metallographic preparation: wet polishing with SiC papers from 200 to 4000 grit size, dry polishing with diamond paste 3 μm and 1 μm , finished with vibratory polishing.
- **AGH/L-GIT:** Specimens were cut using a micro-cutting machine and mounted in a cold conductive resin. They were grinded using 500, 800, 1200 and 2500 SiC

papers. Subsequently, they were polished with 3 microns (MD-DAC pad) and 1 micron (MD-NAP pad) diamond suspensions, followed by OPA (MD-Nap pad) and OPS (MD-Chem pad).

- **LFT:** Sample cutting employing wire EDM, sample mounting in a conductive resin for EBSD, and standard metallographic preparation by wet grinding (3 min P240, P600, and P1200 SiC grit papers successively, applying a 25 N force), standard polishing (5 min using a diamond solution of 6 μm and 1 μm successively, applying a 25 N force; and 5 min using an alumina suspension solution, applying a 25 N force) and final 4 h of vibratory polishing.
- **MU:** Sample cutting employing wire EDM, sample mounting in a conductive resin for EBSD, and standard metallographic preparation by wet grinding (3 min P240, P600, and P1,200 SiC grit papers successively, applying a 25 N force), standard polishing (5 min using a diamond solution of 6 μm and 1 μm successively, applying a 25 N force; and 5 min using an alumina suspension solution, applying a 25 N force) and final 4 h of vibratory polishing.
- **IBF:** Specimens were cut using diamond wire cut and cold mounted in conductive resin. Then, they were ground using 320 SiC papers for 1 min and 2500 SiC papers for 2 min, polished with 3 microns (MD-DAC pad) for 3 min, 1 micron diamond suspensions (MD-NAP pad) for 3 min and colloidal silica of OPS (MD-Chem pad) for 4 min. Finally, the samples were vibratory polished with colloidal silica of OPU for 4 h.

Once the samples were prepared, EBSD scans were conducted at each participating research centre. Despite the EBSD analysis being performed at different locations, identical EBSD parameters were defined for all scans to minimize variations resulting from differing EBSD settings. The EBSD parameters used in this study are listed in Table 5, in which both the parameters for the GG and DRX analysis are specified. The Grain Orientation Spread (GOS) parameter was selected to identify the recrystallized grains on the DRX samples. The GOS parameter is defined as the orientation difference between one pixel and the mean grain orientation:

$$\text{GOS} = \frac{1}{N-1} \frac{1}{N} \sum_{i=1}^N \sum_{j=1}^N \theta_{ij}, i \neq j \quad (2)$$

Table 5 EBSD parameters used by all the research centres participating in this ESAFORM Benchmark project

Area GG/DRX [μm^2]	Step size GG/DRX [μm]	HAGB threshold [$^\circ$]	Detwinning angle tolerance	DRX threshold
3600 \times 2700 / 300 \times 300	3 / 0.15	10	60 $^\circ$ ($\pm 5^\circ$) < 111 >	GOS > 2 $^\circ$ \rightarrow No RX GOS < 2 $^\circ$ \rightarrow RX

GG Parameters for grain growth analysis. DRX Parameters for dynamic recrystallization analysis, HAGB high angle GB

Each grain has a discrete GOS value, which represents the mean geometrically necessary dislocation (GND) density of a grain. The main advantage of the GOS parameter is that it does not depend on the step size used for the EBSD scan [33].

In this study, grains with a GOS misorientation lower or equal to 2° were thus considered as recrystallized grains, and those with a GOS higher than 2° as non-recrystallized grains. The microstructures were also cleaned of their twin boundaries.

Once the EBSD scans were completed at all research centres, the EBSD files were uniformly post-processed using the MTEX Matlab toolbox [43, 44], an open-access toolbox for microstructural analysis. All files were processed with the same script to ensure consistency and avoid discrepancies arising from different post-processing strategies. This approach was adopted to maintain uniformity in the final microstructural results, though no separate analysis was conducted to evaluate the impact of the EBSD post-processing on the outcomes.

In this MTEX script, a threshold of a minimum of 10 pixels per grain and a minimum grain diameter of $2\ \mu\text{m}$ was set to exclude small imperfections from the EBSD scans that do not constitute actual grains. No additional cleaning or smoothing strategies were applied.

The size of each grain was calculated by converting the area of the grain into the equivalent circle diameter (ECD) by the relationship:

$$\theta_i = \sqrt{\frac{S_i}{\pi}} \quad (3)$$

where θ_i and S_i are the equivalent circle diameter and grain surface of the i^{th} grain, respectively. The mean grain size was calculated as:

$$\langle \theta \rangle = \frac{1}{N} \sum_{i=1}^N \theta_i, \quad (4)$$

where N is the total number of analysed grains.

The average recrystallized grain size was calculated to characterise the DRX phenomena under each thermomechanical condition. To this end, as mentioned previously, the recrystallized and non-recrystallized grains were classified based on the GOS misorientation of the grains in the area of analysis, see Table 5.

Once the recrystallized grains were identified, the average recrystallized grain diameter was calculated via:

$$\langle \theta_{RX} \rangle = \frac{1}{N_{RX}} \sum_{i=1}^{N_{RX}} \theta_{RX} \quad (5)$$

where θ_{RXi} is the equivalent circle diameter of the i^{th} recrystallized grain, and N_{RX} is the total number of recrystallized grains.

Finally, the recrystallized fraction was calculated as follows:

$$X_{RX} = \frac{\sum_{i=1}^{N_{RX}} S_i}{S_{\text{tot}}} \quad (6)$$

where S_i is the area of the i^{th} recrystallized grain and S_{tot} is the total analysed area.

EBSD location and magnification influence

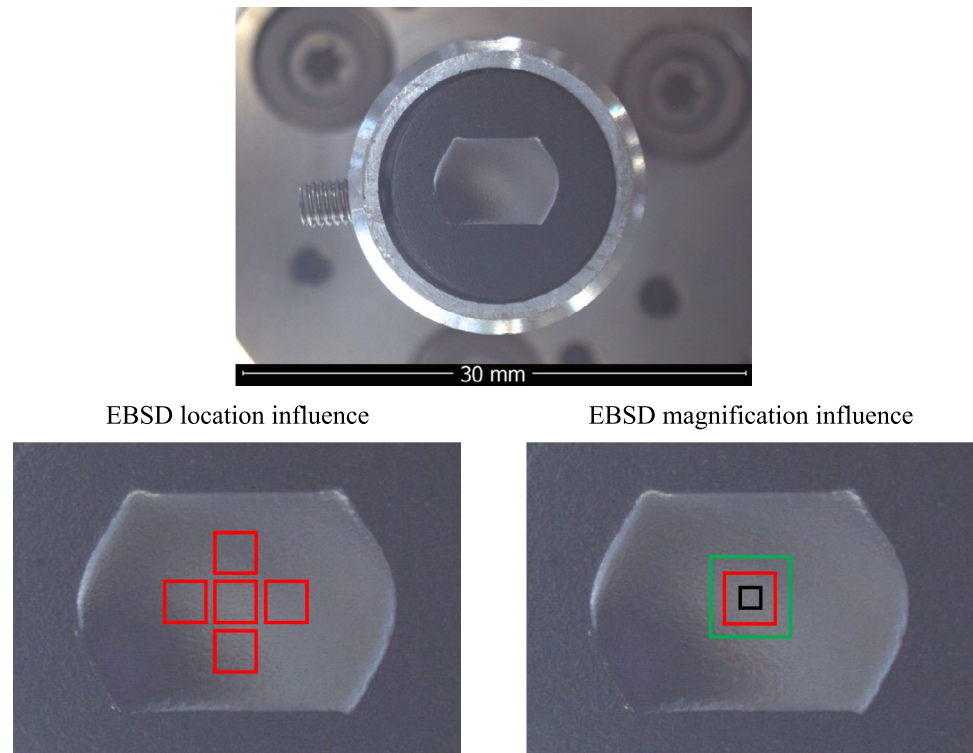
A study was conducted to evaluate the influence on the DRX results of both the location and magnification selected for EBSD scans (Fig. 15). As previously mentioned, EBSD analyses were performed at the centre of the tested samples. However, accurately selecting the exact central points in the SEM can be challenging. This study aimed to evaluate the potential errors introduced by the selected location and magnification during EBSD scanning. For this investigation, one of the samples tested in the dilatometer at MU for DRX analysis was used ($\varnothing 5\text{mm} \times 10\ \text{mm}$). The sample size was the smallest tested in the benchmark, making it the most likely to exhibit errors arising from the selection of the central zone for EBSD scanning. Moreover, the samples tested in the dilatometer showed the biggest friction values ($m=0.8$), therefore, the strain gradient in the cross-section should also be the biggest of all the tested cases.

To analyse the influence of the selected location for EBSD scans, a systematic approach was followed. Initially, the central point of the sample was selected, and an EBSD scan was conducted with a magnification of $\times 350$ and a step size of $0.3\ \mu\text{m}$, covering an area of $300 \times 300\ \mu\text{m}^2$. Following this initial scan, four additional scans were performed using the same EBSD parameters. These scans were conducted at four different locations: up (U), down (D), left (L), and right (R) from the central (C) point, each at a distance of 300 microns from the centre, see Fig. 16.

To analyse the influence of selected magnification, additional EBSD scans were conducted in which the central point of the sample was consistently maintained, see Fig. 17. Building upon the initial scan performed at a magnification of $\times 350$ (covering an area of $300 \times 300\ \mu\text{m}^2$), two further scans were performed. One scan employed a higher magnification of $\times 500$ (B) with a scanned area of $100 \times 100\ \mu\text{m}^2$, and another used a lower magnification of $\times 250$ (S) with a scanned area of $500 \times 500\ \mu\text{m}^2$. The step size remained constant at $0.3\ \mu\text{m}$ for all scans.

Once the EBSD scans were performed, the grain size and recrystallized fraction results were calculated following the methodology explained previously in this section (Eq. 1, 2, 3, and 4). The results of both the EBSD location and magnification studies are presented in Table 6. The findings reveal that the chosen location for EBSD analysis significantly impacts the recrystallized fraction (X_{RX}) results.

Fig. 15 Graphical representation of the two studies carried out to analyse the influence of EBSD location and the EBSD magnification on the DRX results. The sizes of the scanned areas depicted as red, black, and green rectangles are not indicative of the actual scanned areas; they are included for clarity and illustration purposes only



In the central zone, a recrystallized fraction of 0.41 was observed, contrasting with a fraction of 0.31 in both upper and lower locations. The influence appears less pronounced in the horizontal plane, with recrystallized fractions of 0.38 and 0.35 in the left and right locations, respectively. This discrepancy aligns with the lower equivalent strain levels experienced in the upper and lower zones due to the friction and heat transfer with tools during the uniaxial compression test, as illustrated by the virtual twin simulations ("Virtual twin of experimental tests" section). Conversely, the mean grain size and the mean recrystallized grain size exhibit minimal variation based on location, with maximum differences of 0.22 μm and 0.1 μm , respectively. Hence, it can be deduced that the precise centering of the EBSD location in the vertical plane holds greater significance for investigating DRX kinetics than in the horizontal plane.

Regarding the influence of the selected magnification for the EBSD scan, the results indicate minimal variation in both the recrystallized fraction and mean grain size across the three magnifications studied ($\times 500$, $\times 350$, $\times 250$). For the recrystallized fraction, a negligible difference of 1% was observed among the three magnifications. Similarly, the mean grain size and mean recrystallized grain size showed very small differences, with maximum deviations of 0.11 μm and 0.06 μm , respectively. Despite the results revealing only slight differences, care must be taken to avoid excessively high magnifications, resulting in smaller analysed areas and increasing the risk of obtaining non-representative

results. In this study, an intermediate magnification of $\times 350$ was selected for all DRX scans, covering an area of $300 \times 300 \mu\text{m}^2$. This magnification was chosen because it offered the best balance between scanning time and the representativeness of the results.

While this study offers valuable insights, additional extensive research covering a wider range of cases is essential to strengthen the conclusions. Nevertheless, the findings indicate that any observed differences are not primarily due to the EBSD analysis, at least with regard to the grain size results. Moreover, discrepancies in the recrystallized fraction are relatively minor, especially considering that the smallest sample size with the biggest friction tested in this ESAFORM 2023 benchmark project was analysed—the sample of $\text{Ø}5\text{mm} \times 10\text{mm}$ tested in the dilatometers at MU, with a friction of $m=0.8$, which are similar to the ones used by IBF and HER. It is worth noting that all other samples tested in the remaining research centres are larger and with smaller friction values; thus, any differences arising from the EBSD scan are expected to be even smaller.

Results and discussion

This section presents the results and the discussion of GG, DRX, and the characterisation of the thermomechanical behaviour of Alloy 625 obtained from the experimental tests and numerical analyses conducted according to the

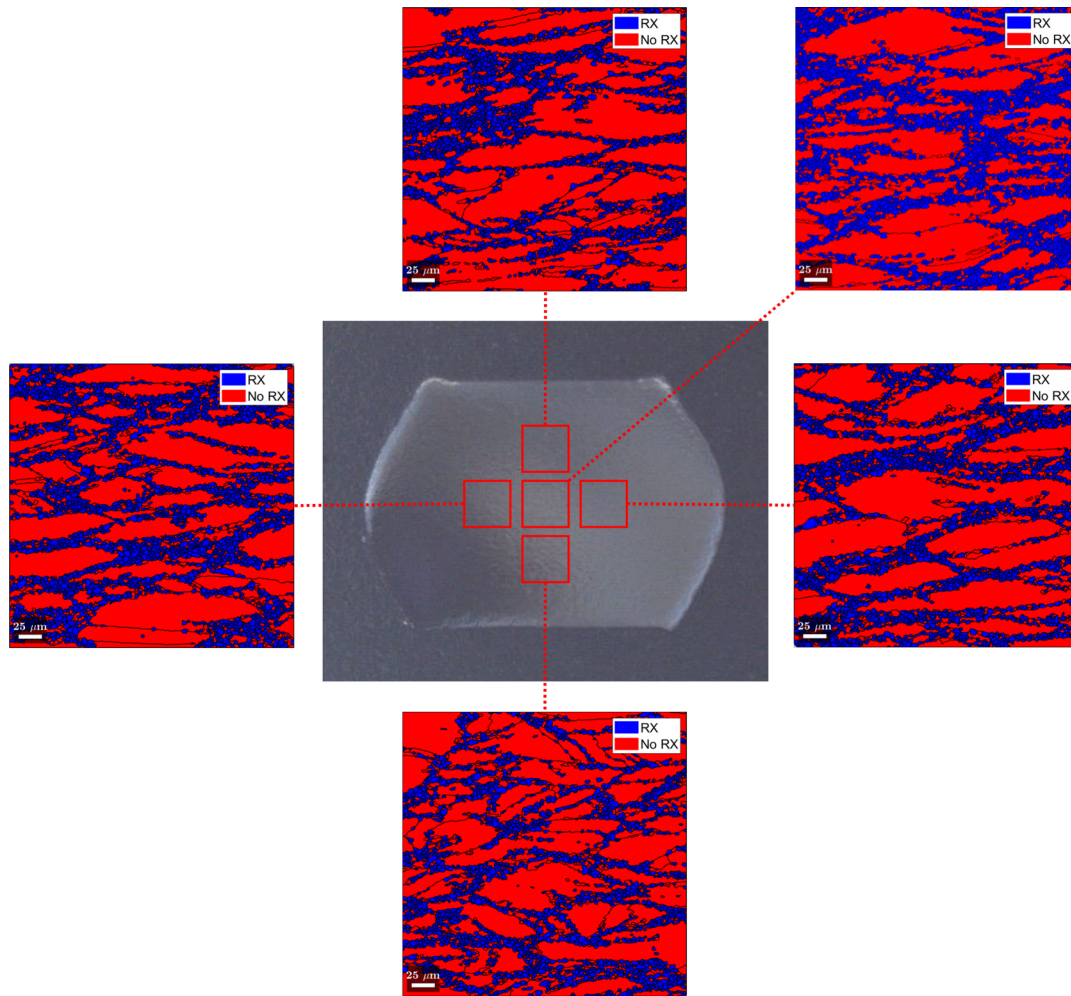


Fig. 16 EBSD micrographs of the five analysed locations. Recrystallized (RX) and non-recrystallized (No RX) grain populations are depicted in blue and red colours, respectively. *The sizes of the*

scanned areas depicted as red rectangles are not indicative of the actual scanned areas; they are included for clarity and illustration purposes only

methodology described in "[Material and experimental procedure](#)" section.

GG kinetics

Figure 18 presents the experimental results of GG in Alloy 625 at 1,150°C using various heating technologies. Radiative furnaces were utilized at both CEMEF and MU, an induction-heated dilatometer was used at MU, and a Gleeble with Joule heating was employed at AGH/L-GIT. Mean grain sizes were calculated using Eq. (1).

The results demonstrate a clear effect of the heating technology on GG behaviour. The Gleeble with Joule heating resulted in significantly higher GG kinetics, followed by the dilatometer with induction heating, which exhibited a moderate grain growth rate. The radiative furnaces showed the smallest GG rate. At the longest holding time (120 min), the mean grain size achieved was 298 μm using Joule heating

in the Gleeble, 170 μm using induction heating, and 118 μm and 106 μm using radiative furnaces at CEMEF and MU, respectively.

EBSD crystallographic orientation maps of samples heat-treated using the three different heating technologies are presented in Fig. 19. These images clearly illustrate the differences in GG behaviour observed in Fig. 18 as holding time increases.

Figure 20 shows the evolution of the sample temperature at the beginning of the GG tests at the different facilities. The temperature was held constant once the testing temperature was reached. The heating rate employed in the dilatometer and the Gleeble was set as constant, while this was not the case in the samples heated in the electrical resistance furnaces, in which a varying heating rate is observed.

Although a slight difference in the initial heating rate exists depending on the employed facility, this factor does not appear to be the main reason for the differences observed

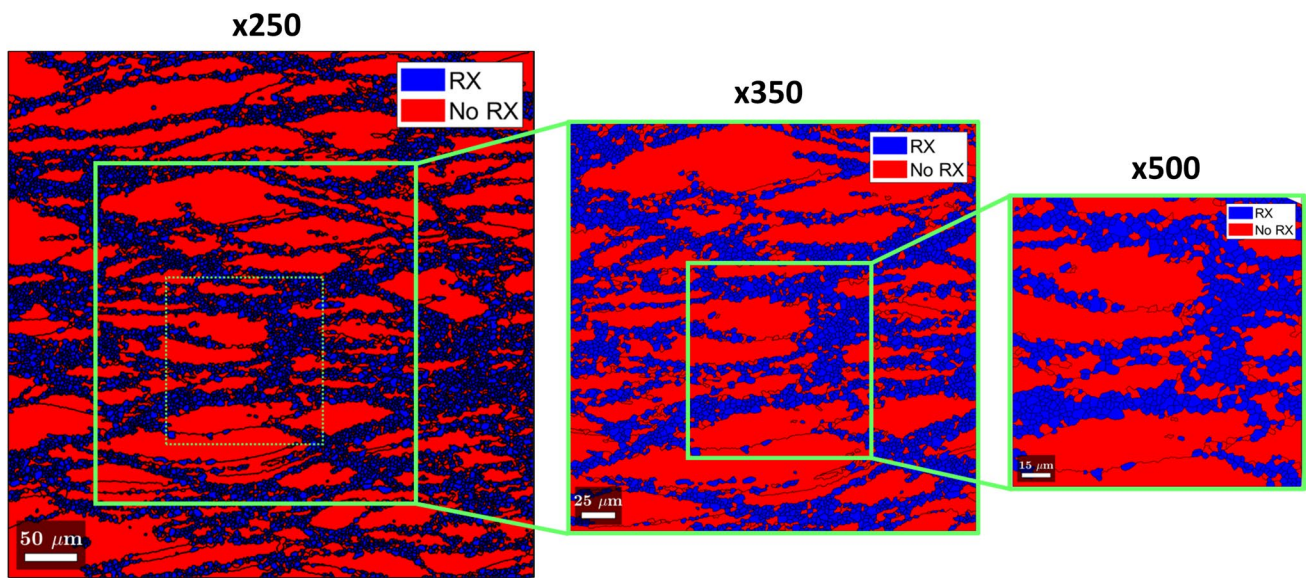


Fig. 17 EBSD micrographs of the central location of the same sample at various magnifications. Recrystallized (RX) and non-recrystallized (No RX) grain populations are depicted in blue and red colours, respectively

Table 6 Results of the EBSD location and magnification influence study

	Case	Magn	Area [μm^2]	Step size [μm]	Mean grain size ($\langle\theta\rangle$) [μm]	DRX fraction (X_{RX}) [-]	DRX grain size (θ_{RX}) [μm]
Location influence	Centre (C)	$\times 350$	300×300	0.3	3.77	0.41	3.38
	Up (U)				3.84	0.31	3.30
	Down (D)				3.99	0.31	3.38
	Left (L)				3.86	0.38	3.41
	Right (R)				3.84	0.35	3.40
Magnification influence	Big (B)	$\times 500$	100×100	0.3	3.88	0.40	3.44
	Centre (C)	$\times 350$	300×300		3.77	0.41	3.38
	Small (S)	$\times 250$	500×500		3.77	0.41	3.38

Magn. = Magnification

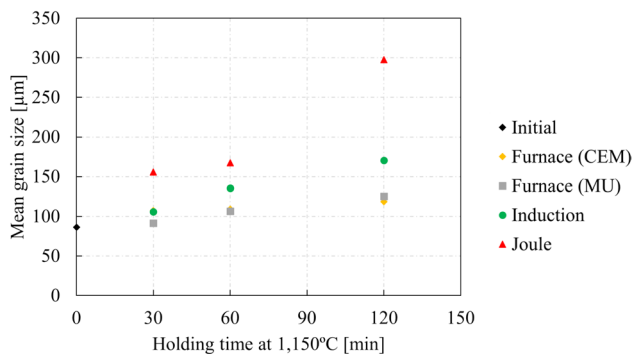


Fig. 18 GG of Alloy 625 at 1,150°C using diverse heating technologies. *Furnace = Radiative furnace* | *Induction = Dilatometer with induction heating* | *Joule = Gleeble with joule heating*

in the GG evolution. Even if samples tested in the furnaces reached the testing temperature approximately 3 min later than samples tested in the dilatometer and the Gleeble, the difference is relatively small compared to the tested holding times (30 min, 60 min and 120 min). Moreover, as samples were homogenised before the grain growth tests (30 min at 1150°C), the effect of the heating rate on the grain growth evolution results appears to be negligible.

Based on the results obtained from the GG analyses, the authors conclude that the heating technology has a clear effect on the grain size evolution, with more pronounced differences observed at longer holding times. In this analysis no deformation was applied to the samples and the heating technology was the only variable that could affect

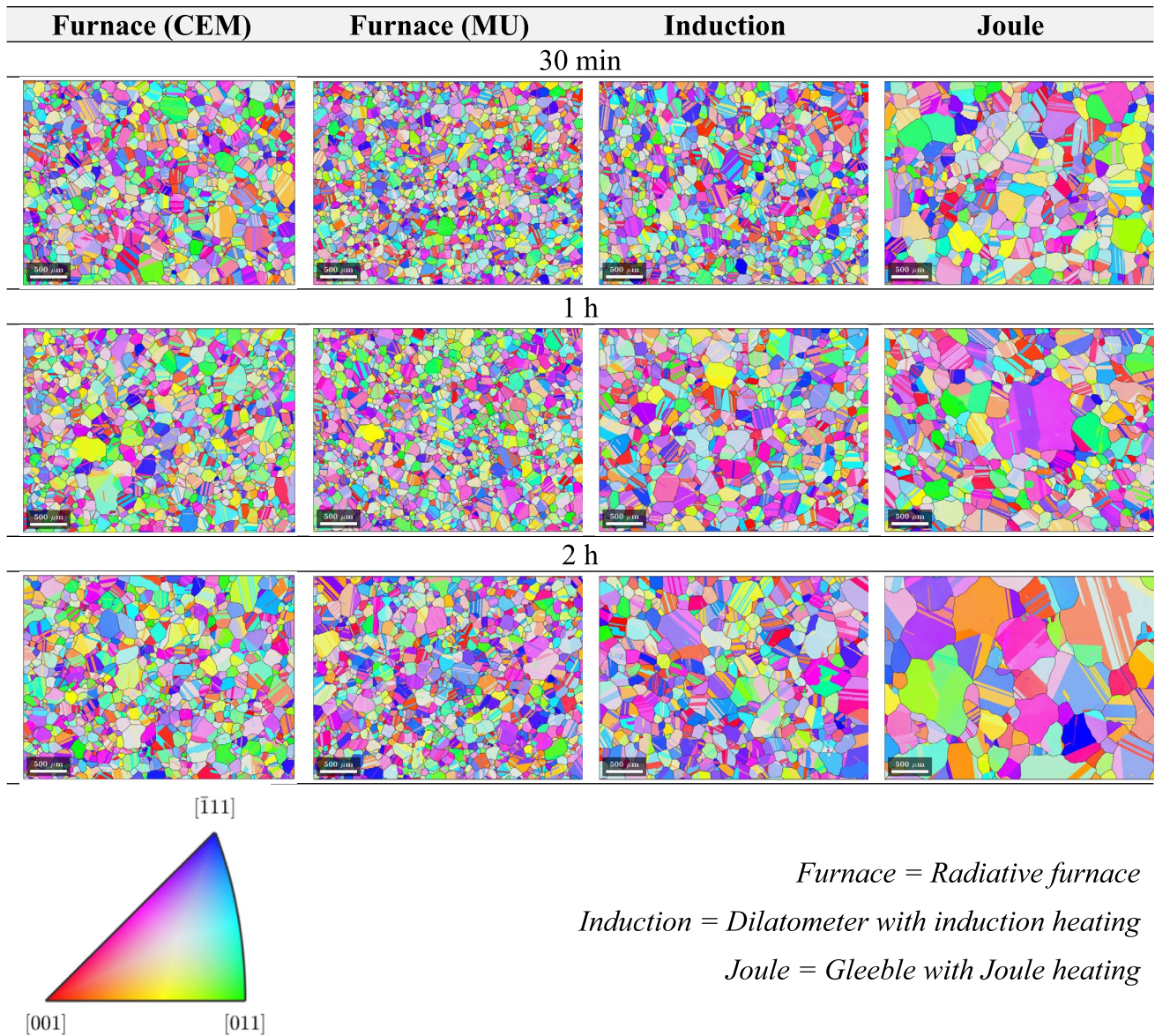


Fig. 19 Crystallographic orientation maps of samples heat treated using diverse heating technologies for grain growth analysis at 1,150°C and different holding times (same magnification in all micrographs)

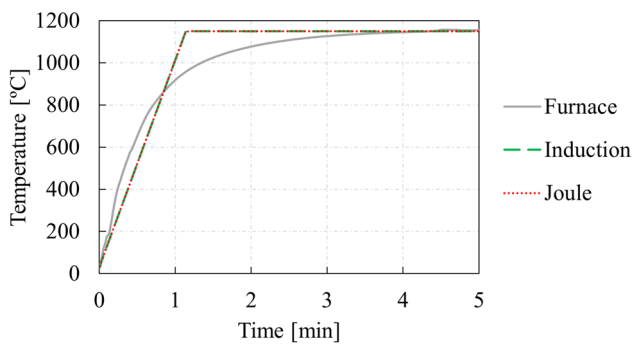


Fig. 20 Heating curves for the grain growth tests at the different facilities

the microstructural evolution. Therefore, it is evident that Joule heating promotes the fastest GG compared to both induction heating and electrical resistance furnace heating, consistent with the findings of Nicolaÿ et al. (2021) and Rheinheimer et al. (2018) mentioned in the introduction. Furthermore, induction heating exhibits higher grain growth kinetics than resistance furnace heating, which results in the slowest grain growth. Finally, except for the Joule heating case, all the curves seem to follow a classical Burke & Turnbull regime [45] in $K\alpha$ with α close to 0.5. It should be noted that the microstructure area analysed in the sample heat-treated for 2 h using Joule heating contained only a few grains, meaning the quantitative mean

grain size results may not be fully representative. An even larger mean grain size would likely be expected, as the grains cut in the edges of the analysed area may result in a slightly smaller mean grain size. An even larger mean grain size would likely be expected, as grains cut at the edges of the analysed area may result in a smaller mean grain size.

In-situ GG results

To better understand the previous results in terms of temporal effects, *in-situ* measurements offer a unique possibility to gain real-time insight into the grain evolution within the material during the thermomechanical processing.

The samples employed in this analysis had not been homogenized; thus, the experiment was started with a homogenization treatment, followed by the heating and deformation cycle. At room temperature, detector image #4 in Fig. 21 shows homogeneous diffraction rings of a single-phase material with a face-centred cubic crystal structure; the roughness value is 0.021. When a temperature of 1150 °C is reached after 66 s; the corresponding detector image #15 shows spots on the diffraction rings, which means that the grain size started to increase. After 180 s, a strong increase of the roughness of the (311) ring is observed. Image #37 shows that the rings are not homogeneous anymore and strong spots have been formed, which correspond to the presence of large grains. The roughness increases until

1000 s (16.67 min) and it remains constant until the homogenisation heat treatment of 1800s (30 min) is finished.

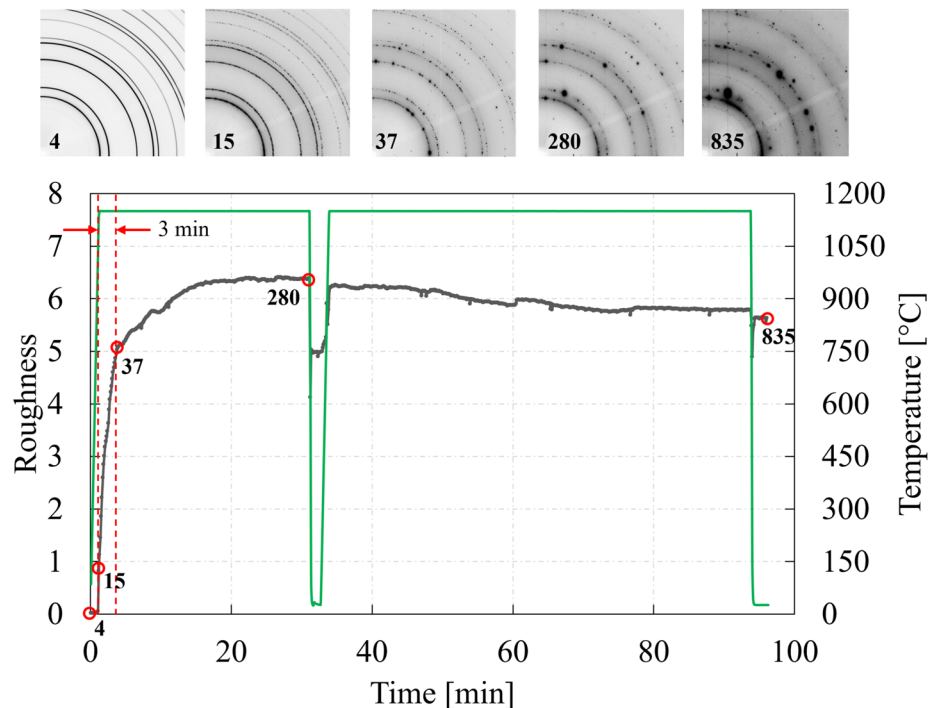
After the homogenisation heat treatment, and after a holding time of 5 min at room temperature, the *in-situ* GG test was performed at 1150°C for 60 min. During the final holding time at 1150°C, a slight decrease of the roughness was observed. The roughness drop during the GG heat treatment does not represent a grain size decrease, as grains continue to grow when held at 1150°C, see Fig. 18. The reasons for this effect could not be explained.

The *in-situ* grain growth tests indicate that the strongest grain growth occurs in the first 180 s of the homogenisation treatment, and the subsequent grain growth is relatively slow. This behaviour is quite typical in pure grain growth after recrystallization and rapid quenching, where the faster initial kinetics correspond to the equilibration of triple junctions, followed by an increasingly slower regime, as depicted by the Burke & Turnbull regime. It is important to note that this behaviour depends on the way the samples are produced, i.e. on the initial deformation state and any previous heat treatments.

Thermomechanical characterisation

This section presents the experimental thermomechanical results of Alloy 625 obtained from the uniaxial compression tests conducted at the different testing facilities. The tests were carried out at 1050°C and macroscopic true strain rates of 0.01 s⁻¹, 0.1 s⁻¹ and 1 s⁻¹, following

Fig. 21 Roughness of the (311) diffraction ring (the fourth ring) as a function of time. One quarter of a detector image is shown for the start at RT (image #4), when 1150 °C is reached (#15), at the end of homogenization (#280) and at the end of the annealing time (#835)



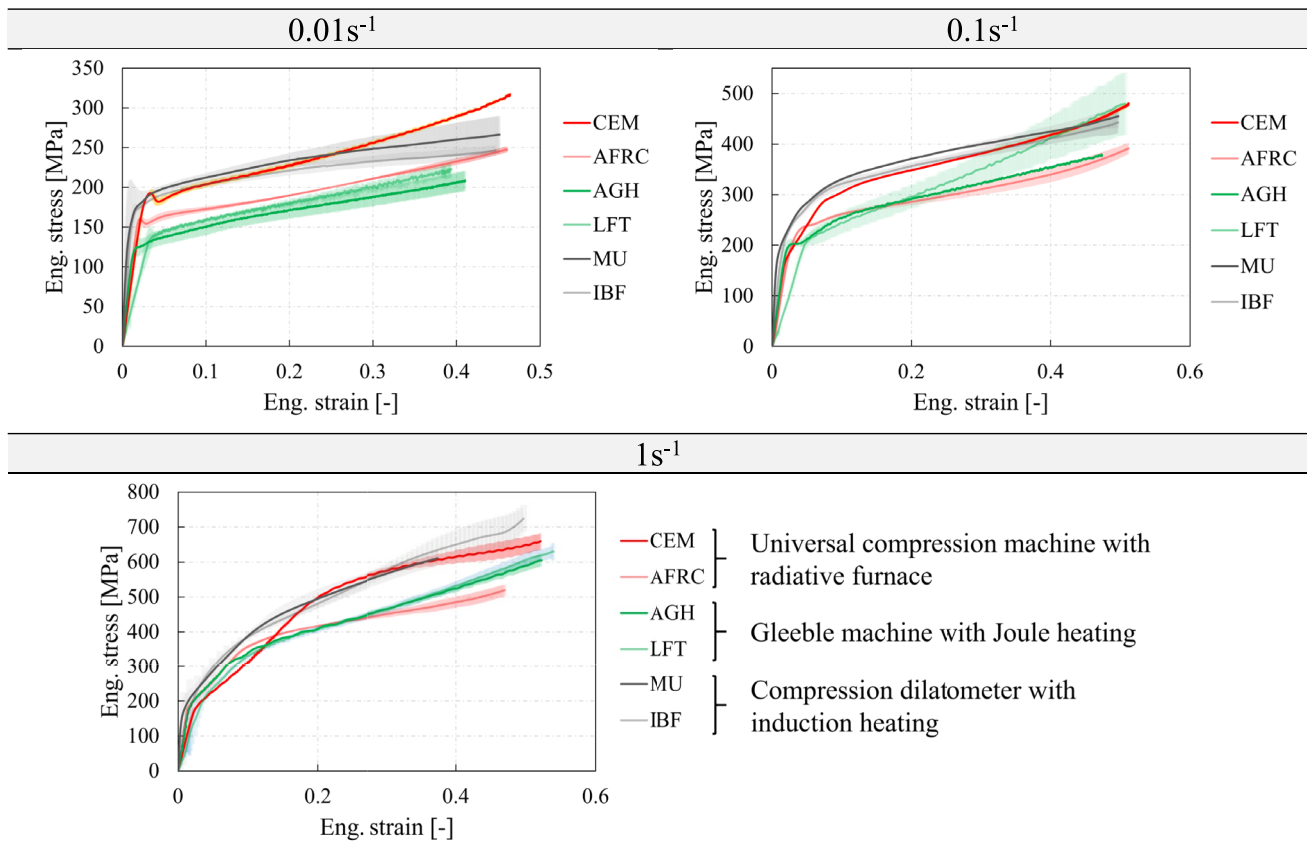


Fig. 22 Engineering stress–strain curves of alloy 625 obtained from compression tests performed at 1,050°C and macroscopic strain rates of 0.01 s^{-1} , 0.1 s^{-1} and 1 s^{-1}

the methodology outlined in "[Compression tests to study the thermomechanical behaviour and DRX kinetics](#)" section. Figure 22 presents the experimental engineering stress–strain curves of Alloy 625 at the three tested strain rates. The mean value was computed based on three repetitions conducted under each condition. Dispersion among the three repetitions is also depicted to illustrate the variability in each testing facility.

The results show significant variability, with discrepancies of up to 200 MPa observed in some cases. Stress–strain curves obtained from tests conducted at CEMEF using a universal compression machine, and in dilatometers at MU and IBF, show slightly higher stress values across all tested strain rates. Conversely, tests conducted in the universal compression machine at AFRC, and in Gleeble machines at AGH/L-GIT and LFT, show lower stress values. These latter three cases exhibit a similar trend, except for the test at LFT at a 0.1 s^{-1} strain rate, which presents a notably higher hardening rate. It should be noted that the tests at LFT were intentionally performed at a constant speed rather than a constant strain rate, as it is explained later in this section. Overall, the curves demonstrate a comparable trend in terms of hardening rate, except for the dilatometer curves at MU

and IBF at a strain rate of 0.01 s^{-1} , which exhibit slightly lower hardening rates at higher strain levels.

In terms of repeatability, the tests show high consistency when considering the results from each research centre independently. Regarding repeatability based on the type of facility, both the compression dilatometers at MU and IBF, as well as the Gleeble machines at AGH/L-GIT and LFT, exhibit exceptional agreement (except LFT at 0.1 s^{-1}). In contrast, the curves obtained from tests conducted in the universal machines at CEMEF and AFRC, despite being similar facilities with comparable heating technologies, show significant differences. It is noteworthy that the deformation dilatometers at MU and IBF are identical facilities, while the Gleeble machines at AGH/L-GIT (3800 series) and LFT (3500 series) are also closely comparable. Hence, it is reasonable to anticipate consistent results between these two facilities. On the other hand, the universal machines at CEMEF and AFRC are not identical, as their heating furnaces differ, which contributes to the discrepancies in results. The heating times were also different, with a 5 min heating time at CEMEF and 60 min at AFRC.

The differences observed in the curves depicted in Fig. 22 are not attributed to variation of strain rate, as this parameter

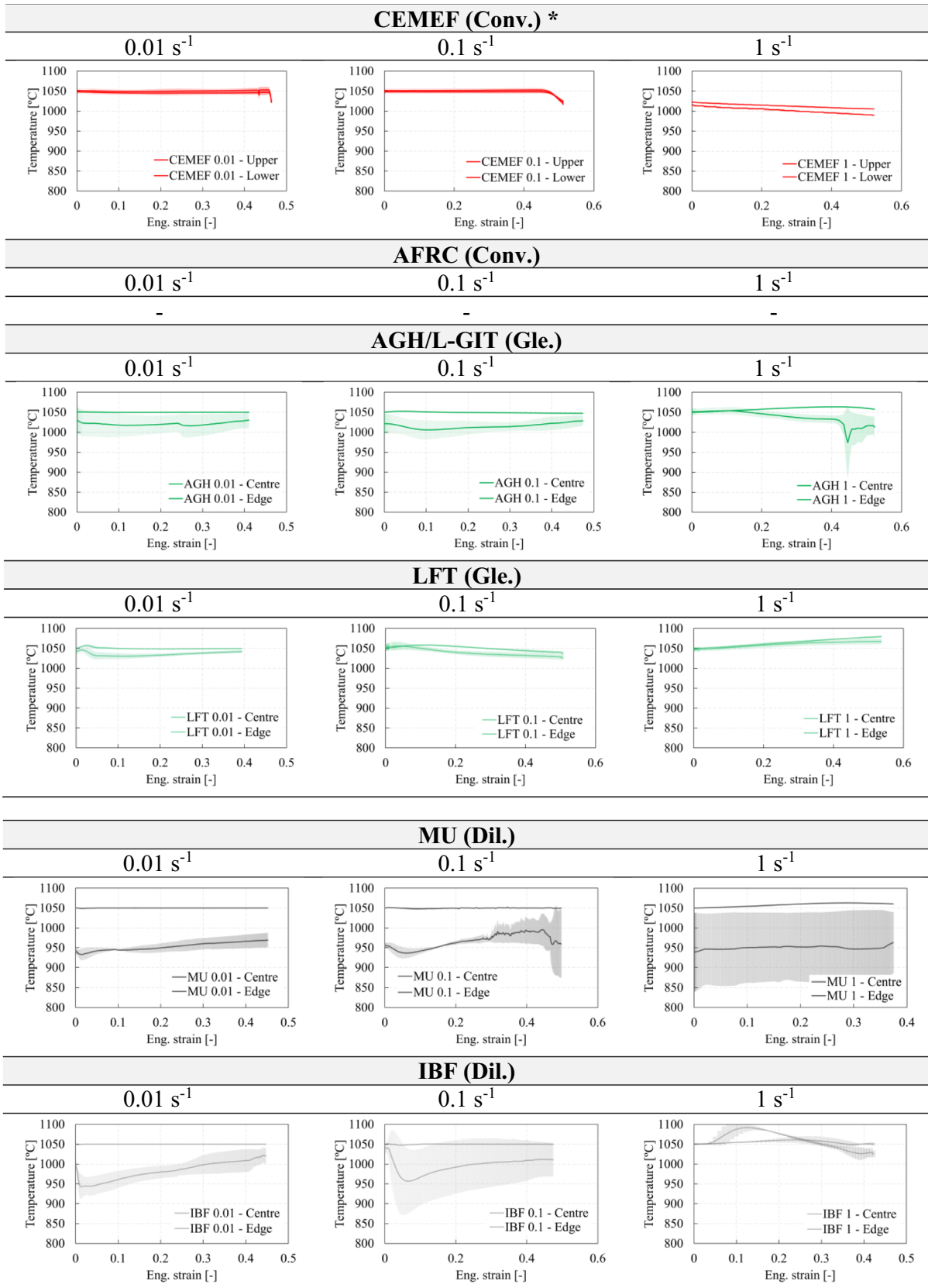


Fig. 23 Experimental temperature measurements acquired from thermocouples attached to the tested samples at the centre and the edge. **In the tests conducted at CEMEF, the thermocouples were not attached to the sample but to the upper and lower tool surfaces. In the case of AFRC, the initial temperature was ensured with thermocouples, but these broke during compression and no temperature evolution results could be acquired*

remained constant and well-controlled during compression in all the employed testing facilities (except in LFT). To explain the differences, the temperature data acquired from thermocouples attached to the samples at the centre and edge (see Fig. 5) are presented in Fig. 23.

In the case of CEMEF, the correct testing temperature was ensured based on thermocouples attached to the upper and lower tool surfaces instead of being directly affixed to the sample, therefore, the results shown in Fig. 23 are not directly comparable with the rest of the testing facilities. In the tests in this research centre, samples were introduced in the furnace and held for 5 min at the testing temperature prior to the start of the compression test. The time employed to heat the samples to the testing temperature was estimated to be sufficient. The final temperature drop observed in the CEMEF tests at 0.01 s^{-1} and 0.1 s^{-1} , belongs to the opening of the furnaces at the end of compression to ensure a fast post-forming quenching. Samples are pushed to a water tank just after the compression finishes. In the case of the tests at 1 s^{-1} , due to the short test duration ($< 1 \text{ s}$), the furnace is opened just before the compression starts to minimise the post-forming quenching time, and that is why the die temperature decreases continuously.

In the case of tests carried out at AFRC, the thermocouples utilized to monitor initial temperature conditions, which were attached to the centre of the samples, broke during deformation. Therefore, although the initial temperature was ensured to be correct, no temperature evolution could be recorded during the compression tests.

Concerning the temperature gradient from the centre to the edge of the tested samples, a discernible gradient is observed in all cases. In the Gleeble machines with Joule heating, the temperature difference from the centre to the edge appears smaller compared to the deformation dilatometers with induction heating. Specifically, the temperature gradient in the Gleeble machines at AGH/L-GIT and LFT is a maximum of 50°C , whereas in the dilatometers at MU and IBF, the gradients are slightly higher, with average maximum differences of 100°C .

In Fig. 24, temperature measurements at the sample centre are compared across all testing facilities and strain rates. Initial sample temperature precision was consistent across all the cases, and temperature control in both dilatometers and Gleeble machines was notably accurate, particularly at the lowest tested strain rates of 0.01 s^{-1} and 0.1 s^{-1} . At the

highest tested strain rate (1 s^{-1}), an increase in temperature is observed, typically attributed to significant adiabatic heating at higher strain rates. The experimental temperature evolution of the tests performed at CEMEF and AFRC are not included, as in the case of CEMEF the temperature of the sample was not measured, and in the case of AFRC the thermocouples broke once the compressions were started and no temperature evolution could be acquired.

The findings of the investigation into the influence of constant and non-constant true strain rates on the engineering stress–strain curve are presented next. As previously outlined, the study aimed to analyse how the consistency of strain rate affects flow behaviour. Identical tests were conducted using the two Gleeble machines involved in the benchmark. At AGH/L-GIT, compression tests were conducted with a constant true strain rate, while at LFT, the same tests were performed with constant speed (not constant true strain rate).

The engineering stress–strain results are depicted in Fig. 25a, while the macroscopic true strain rate evolutions are illustrated in Fig. 25b. The latter clearly shows the disparity in strain rates between the two testing approaches. For strain rates of 0.01 s^{-1} and 1 s^{-1} , minimal differences are observed in the engineering stress–strain curves, whereas a significant stress difference is noted at 0.1 s^{-1} . Given the lack of variation in stress between 0.01 s^{-1} and 1 s^{-1} , the disparities observed at 0.1 s^{-1} may not solely be attributed to differences in strain rate evolution. Instead, the discrepancies observed at 0.1 s^{-1} may derive from inaccurate temperature control at this strain rate, as depicted in Fig. 24.

Based on the results presented in this section, the authors suggest that the flow stress scatter observed in Fig. 22 can be attributed to several combined factors, with the most significant being the thermal gradient, friction effects, and the initial microstructure state. Regarding the effect of friction, the literature indicates that higher friction in uniaxial compression tests typically leads to higher flow stresses [46]. However, in the tests performed at CEMEF, where friction was the lowest ($m=0.05$), the flow stress was among the highest observed. This indicates that friction is likely not the main factor responsible for the differences observed in the flow stresses.

Therefore, the primary source of this scatter is likely to be the thermal gradient within the samples at the beginning and during the compression test. Samples tested in dilatometers with induction heating exhibited the largest thermal gradient from the centre to the edges of the sample ($\approx 100^\circ\text{C}$), while those tested in Gleeble machines with Joule heating showed a smaller gradient ($< 50^\circ\text{C}$). In conventional thermomechanical testing machines equipped with an electrical furnace, the thermal gradient should theoretically be minimal, as both the sample and tools are at the same temperature.

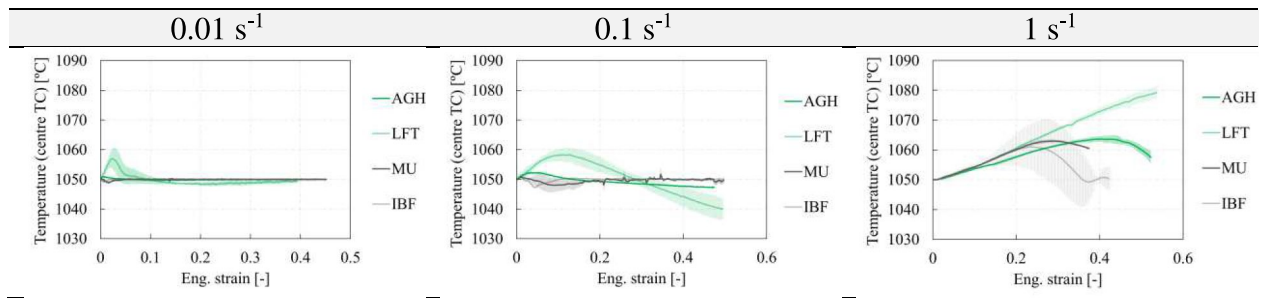


Fig. 24 Temperature evolution at different testing facilities measured using the thermocouple attached to the centre of the tested sample

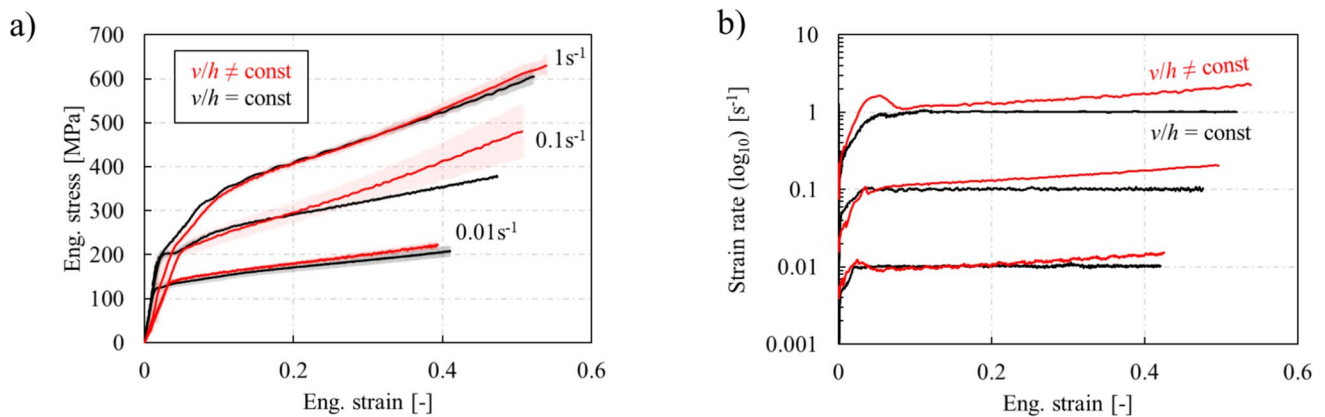


Fig. 25 a) Engineering stress–strain curves of alloy 625 tested in Gleeble machines at constant strain rate (AGH/L-GIT) and constant speed (LFT). b) Macroscopic true strain rate evolution with both testing approaches

Regarding the differences observed between the curves obtained from the two conventional testing machines heated by electrical furnaces at CEMEF and AFRC, the heating furnace and specially the heating time appear to have a significant effect. In the tests conducted at AFRC, samples were heated for one hour, considerably longer than that used in CEMEF (5 min), and this could have affected the initial state of the material prior to the compression. The samples had already undergone homogenisation at 1150°C for 30 min, so the additional grain growth during the 60 min at 1050°C would not have been substantial. However, the initial grain size prior to compression at AFRC was likely larger than at CEMEF, which could have contributed to the observed lower flow stresses. Given the identical heating times in the conventional machine at CEMEF, in the dilatometers at MU and IBF, and in the Gleeble machines at AGH/L-GIT and LFT, the initial microstructure in these cases should be very similar.

The similarity between the flow stress curves obtained at CEMEF and those from the dilatometers is not yet fully understood. Given that the samples tested in the dilatometers had the smallest dimensions ($\varnothing 5\text{mm} \times L10\text{mm}$), the highest friction ($m=0.8$) and the largest thermal gradient from the

centre to the edges of the sample ($\approx 100^\circ\text{C}$), the impact of these factors on the flow curves is expected to be the most significant. Consequently, the flow stress values obtained in the dilatometer tests should be higher than those obtained from tests with thermally homogenised samples at CEMEF. However, this is not the case, as the dilatometer curves show generally comparable flow stresses to those at CEMEF.

In contrast, the flow curves obtained from the Joule-heated Gleeble machines exhibit lower flow stress values compared to those from the tests at CEMEF. The samples tested in the Gleeble machines had a smaller thermal gradient than those in the dilatometer, with a maximum difference of 50°C between the centre and the edges. Given this, the flow stress levels from both CEMEF and Gleeble tests should be comparable, yet this is not the case, with significantly lower flow stress levels in the Gleeble tests. The friction coefficients in both machine types are similar, with $m=0.05$ at CEMEF and $m=0.2$ in the Gleeble machines. This suggests that friction is unlikely to be the primary cause of the observed differences.

In conclusion, it is challenging to attribute the differences observed in the flow stress directly to the employed heating technology (furnace, induction, or Joule heating).

The temperature gradient produced by each heating method, rather than the technology itself, appears to play a more significant role. Nevertheless, the hypothesis that Joule heating may lead to lower flow stresses cannot be entirely dismissed, and it remains as an open question for further investigation.

DRX kinetics

This section presents the dynamic recrystallization results of Alloy 625 obtained from uniaxial compression tests conducted at the different research centres at strain rates of 0.01 s^{-1} , 0.1 s^{-1} , and 1 s^{-1} . The results include the DRX fraction and the recrystallized grain diameter.

The uniaxial compression tests were performed following the methodology described in "Compression tests to study the thermomechanical behaviour and DRX kinetics" section. After the tests were carried out, the samples were prepared for microstructural observation, as detailed in "Metallographic preparation and microstructural analysis"

section. Following the EBSD scans, the DRX results were computed according to the equations described in "Metallographic preparation and microstructural analysis" section.

The DRX volume fractions versus the equivalent strain level in the centre of the samples for the three tested strain rates and for the different testing facilities are presented in Fig. 26. The equivalent strain levels were numerically estimated through inverse simulation using the FORGE® simulation software ("Virtual twin of experimental tests" section).

The well-established DRX trend in the literature indicates that higher strain levels result in higher recrystallized fractions. However, when comparing the DRX fractions obtained in this study across different testing facilities, deviations from this trend are observed, particularly at the lowest strain rates (0.01 s^{-1} and 0.1 s^{-1}). At these strain rates, the results from the Gleeble machines at AGH/L-GIT and LFT show higher recrystallized fraction values that slightly deviate from the overall trend. Similarly, the recrystallized

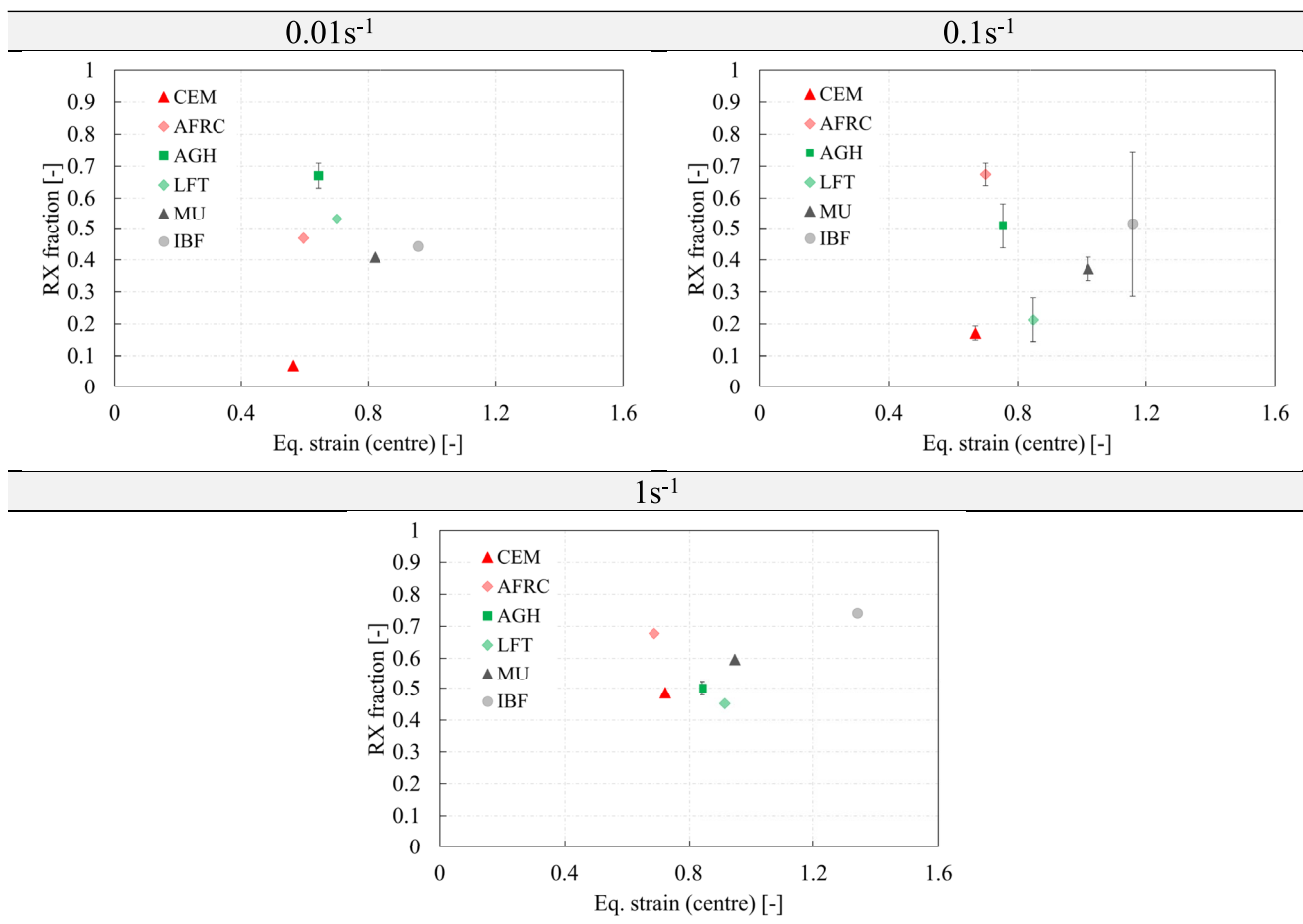


Fig. 26 Recrystallized fraction of alloy 625 obtained from DRX compression tests performed at $1,050^\circ\text{C}$ and macroscopic strain rates of 0.01 s^{-1} , 0.1 s^{-1} and 1 s^{-1}

fractions of the samples tested at AFRC show higher fractions in all the tested conditions.

In all the research centres, for the strain rates of 0.01 s^{-1} and 1 s^{-1} , a single sample was analysed using EBSD, while for 0.1 s^{-1} , three samples were examined to estimate the variability inherent to the EBSD analysis. Overall, relatively small deviations, ranging from 4–14%, were observed across all facilities, except for a significant dispersion of 48% in the three samples tested in the dilatometer at IBF. This unusually high deviation might be attributed to the specific sample zone selected for the EBSD analysis. Given that the samples tested in the dilatometer are the smallest ones ($\text{Ø}5 \times 10\text{ mm}$), the scatter due to EBSD zone selection could be more pronounced, as shown in "EBSD location and magnification influence" section. This conclusion is supported by the significantly lower deviation observed in the tests performed using an identical deformation dilatometer at MU.

Figure 27 presents the average DRX grain diameters for all the analysed cases. The recrystallized grain population was identified based on the GOS number ($\text{GOS} < 2^\circ$), as

detailed in "Metallographic preparation and microstructural analysis" section. According to the literature, the DRX grain size does not evolve beyond the onset of DRX. Therefore, once DRX is initiated, the DRX grain size remains constant independently of the equivalent strain [8].

The results exhibit significant scatter, with samples tested in the Gleeble machines at AGH/L-GIT and LFT, as well as in the universal machine at AFRC, generally showing slightly larger resulting DRX grain sizes. Regarding repeatability among the same types of facilities, the dilatometers with induction heating demonstrate the smallest differences, with DRX grain size variations ranging from $0.27\text{ }\mu\text{m}$ to $1.1\text{ }\mu\text{m}$. The resulting DRX grain diameter differences between the Gleeble machines with Joule heating (AGH and LFT) are slightly larger, ranging from $0.29\text{ }\mu\text{m}$ to $2.14\text{ }\mu\text{m}$. The DRX grain diameters obtained from the tests performed at CEMEF are generally closer to the dilatometer results, whereas the AFRC results show significantly larger DRX grain diameters, especially in the tests conducted at 0.1 s^{-1} and 1 s^{-1} .

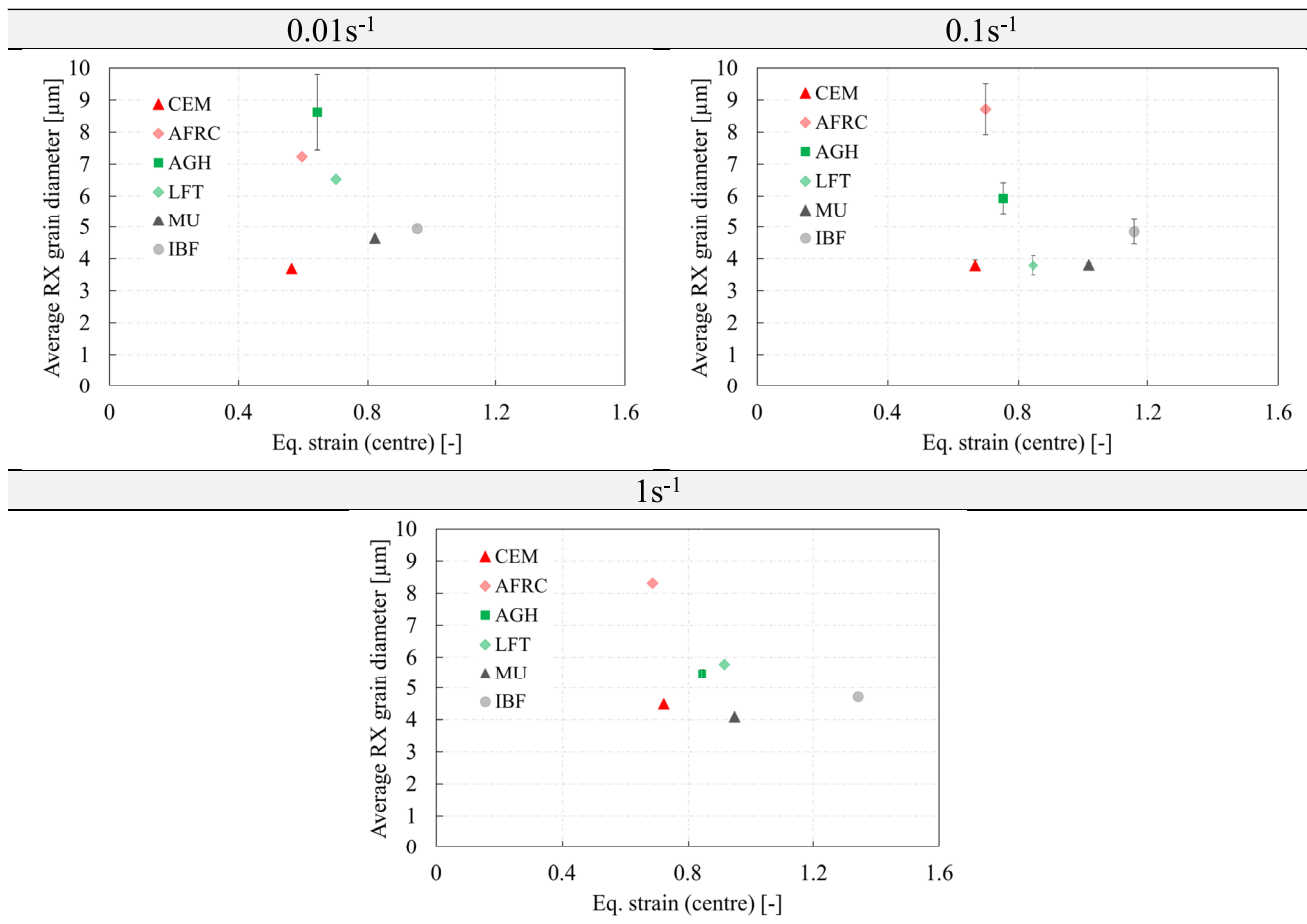
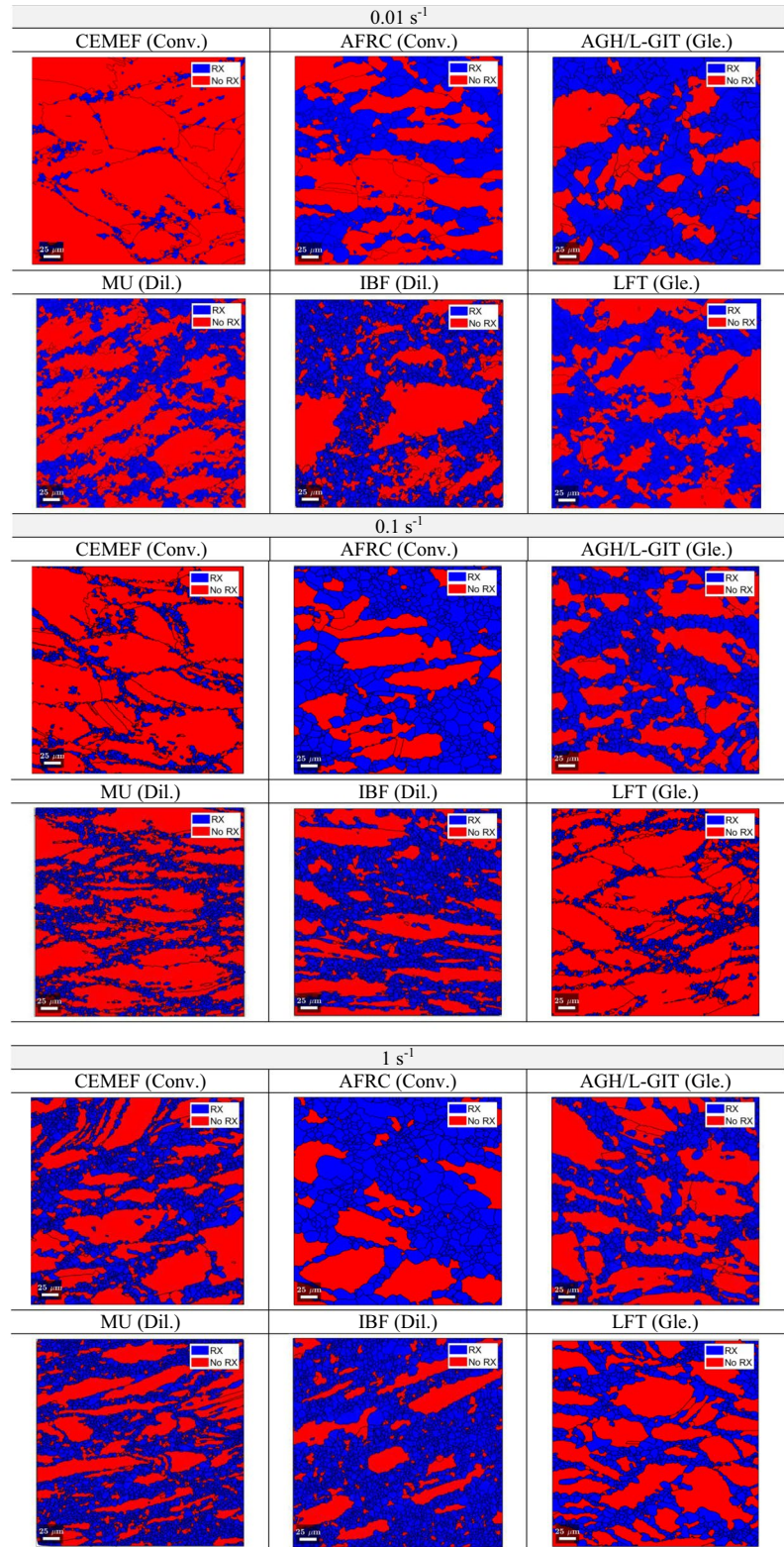


Fig. 27 Recrystallized grain size of alloy 625 obtained from DRX compression tests performed at $1,050^\circ\text{C}$ and macroscopic strain rates of 0.01 s^{-1} , 0.1 s^{-1} and 1 s^{-1}

Fig. 28 Micrographs of alloy 625 obtained from DRX compression tests performed at 1,050°C and macroscopic strain rates of 0.01 s⁻¹, 0.1 s⁻¹ and 1 s⁻¹



Conv. = Conventional compression machine with radiative furnace
 Dil. = Deformation dilatometer with induction heating
 Gle. = Gleeble with Joule heating

The micrographs corresponding to the results depicted in Figs. 26 and 27 are presented in Fig. 28, categorised by strain rate and testing facility. Both grain populations, the recrystallized and non-recrystallized grains, were separated based on the GOS parameter ("[Metallographic preparation and microstructural analysis](#)" section) and are depicted with distinct colour codes. Recrystallized grains are highlighted in blue, while non-recrystallized grains are represented in red.

To provide further insight into the DRX results, the KAM maps for the analysed cases are presented in Fig. 29. KAM maps represent local misorientations within the examined microstructures.

When comparing the KAM maps between equivalent testing facilities, the CEMEF and AFRC cases, which were tested in conventional thermomechanical machines equipped with resistance furnaces, considerably differ. These significant differences may arise from the notable difference in quenching time, which was less than 1.8 s in the tests at CEMEF and increased to 15 s in the tests at AFRC. In the tests at AFRC important post-dynamic evolution is expected to have happened due to the long post-forming quenching time, which explained that all corresponding microstructures present larger recrystallized fractions and recrystallized grains than other ones.

Regarding the KAM maps obtained from the tests performed in the induction-heated dilatometers, results appear to be comparable in all the tested conditions, with similar misorientation values within the recrystallized and non-recrystallized grains. As for the samples tested in the Gleeble machines with Joule heating, maps also show comparable results, with slightly smaller KAM values in the recrystallized grains of the test performed at 1 s^{-1} at LFT.

When comparing KAM maps of the samples tested under same conditions in the different testing facilities, samples tested at CEMEF clearly show the highest KAM values in all the tested conditions, which represents higher dislocation density regions in non-recrystallized grains. When dilatometer and Gleeble maps are compared, in general non-recrystallized grains of samples tested in the dilatometers appear to show slightly higher misorientation regions. This especially occurs at the lowest strain rates (0.01 s^{-1} and 0.1 s^{-1}), with more comparable results in the samples tested at 1 s^{-1} .

The high KAM values observed in the non-recrystallized grains of samples tested at CEMEF clearly represent the strain hardening that takes place before DRX is triggered. The KAM differences observed between the different testing facilities show that the heating technology has an impact on how the grains are strained before DRX is started. Furnace heating appears to promote the highest grain straining, followed by induction heating, which results in higher misorientation values if compared to Joule heating, especially at the lowest strain rates (0.01 s^{-1} and 0.1 s^{-1}). More

comparable results between induction and Joule heating are observed in samples tested at 1 s^{-1} .

In terms of the test duration, samples tested at 0.01 s^{-1} , 0.1 s^{-1} , and 1 s^{-1} , last on average 55 s, 7 s, and 0.8 s, respectively. The fact that the heating technology has an impact on DRX kinetics, especially at the lowest strain rates, appears to be in agreement with the results observed in "[GG kinetics](#)" section, in which a clear effect of the heating method was observed regarding the grain growth evolution. Tests performed in the Gleeble machines (Joule heating) at the strain rates of 0.01 s^{-1} and 0.1 s^{-1} , show higher recrystallized fractions (Fig. 26) and bigger recrystallized grain sizes (Fig. 27), a similar tendency as observed in the GG tests. At the strain rate of 1 s^{-1} , in which the test duration is the shortest, the differences between heating types in both DRX fraction and recrystallized grain size are significantly smaller.

When the results of both Gleeble machines are compared, results from LFT tests show smaller DRX fractions and smaller recrystallized grain sizes than AGH/L-GIT results. It is important to highlight that, as compression tests in LFT were performed with the tool kinematics set as constant speed instead of a constant macroscopic strain rate, the test duration was shorter than in AGH/L-GIT. The 0.01 s^{-1} tests in LFT and AGH/L-GIT last 41 s and 55 s, respectively, and the 0.1 s^{-1} tests last 4.6 s and 7.5 s, respectively.

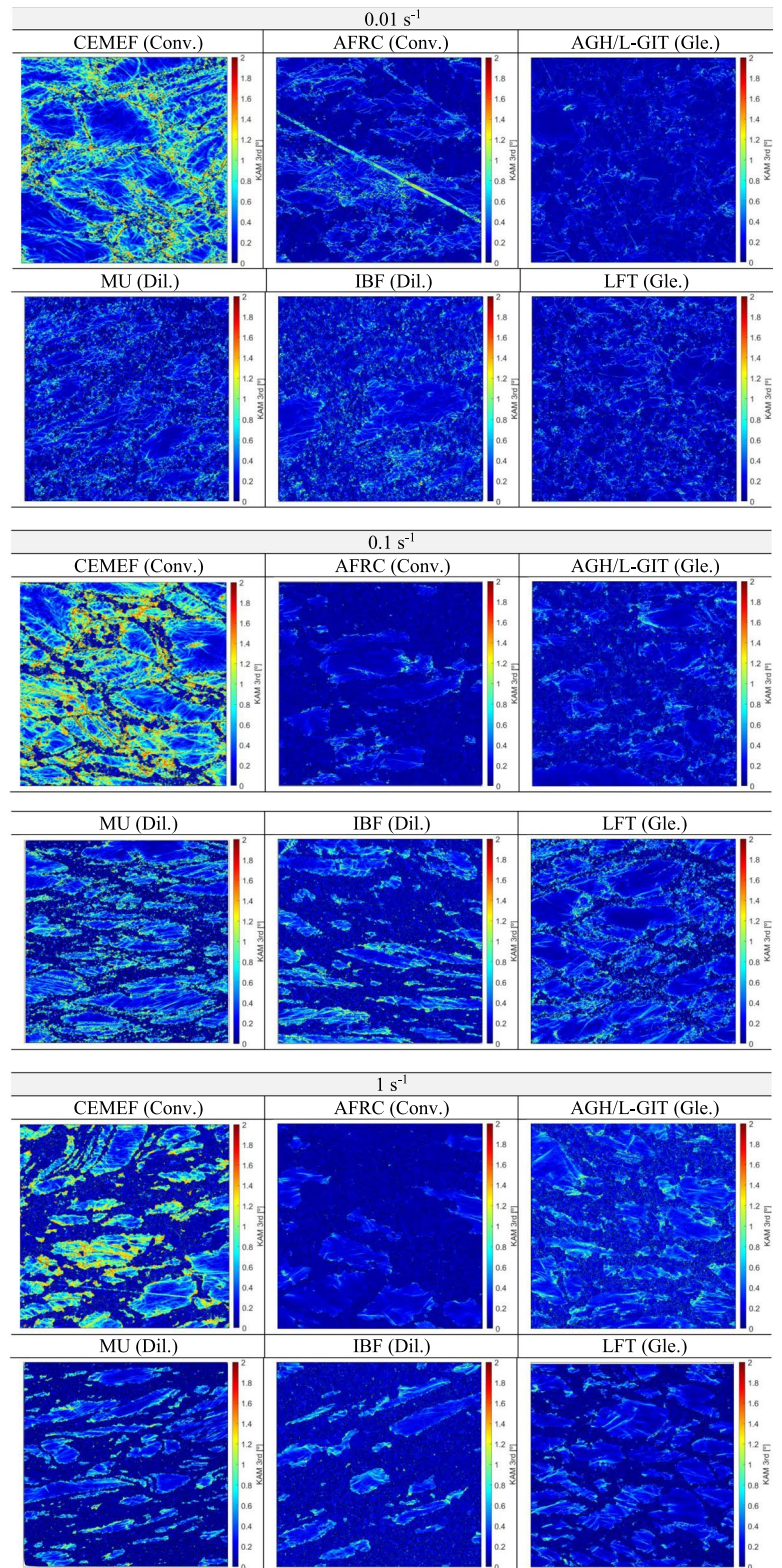
Although more conditions should be tested and more repetitions should be performed to make more robust conclusions, considering the results obtained from the DRX analysis, the hypothesis that Joule heating promotes faster DRX kinetics cannot be rejected, especially at low strain rate tests. At these strain rates, the test duration is extended, making the influence of Joule heating on microstructural evolution potentially more significant.

***In-situ* DRX results**

Similar to the GG analysis in "[In-situ GG results](#)" section, *in-situ* compression tests were conducted at the synchrotron to obtain real-time insights into the DRX evolution occurring during deformation.

The diffraction rings exhibit the typical spottiness after the homogenization treatment leading to a roughness value of around 6, representative of a distribution of coarse grains. The corresponding detector images (one-quarter) are displayed in Fig. 30. The roughness starts to decrease immediately after the onset of deformation. R reaches a value of 0.3, which is 5% of the starting value, about 4.1 s (0.01 s^{-1}), 0.35 s (0.1 s^{-1}), and 0.1 s (1.0 s^{-1}) after it starts to drop. At this point, a visual inspection of the diffraction images confirms the reduction in spottiness. The roughness continues to drop before coming to a plateau where little happens until the end of the deformation.

Fig. 29 KAM maps of alloy 625 obtained from DRX compression tests performed at 1,050°C and macroscopic strain rates of 0.01 s⁻¹, 0.1 s⁻¹ and 1 s⁻¹



Conv. = Conventional compression machine with radiative furnace
 Dil. = Deformation dilatometer with induction heating
 Gle. = Gleeble with Joule heating

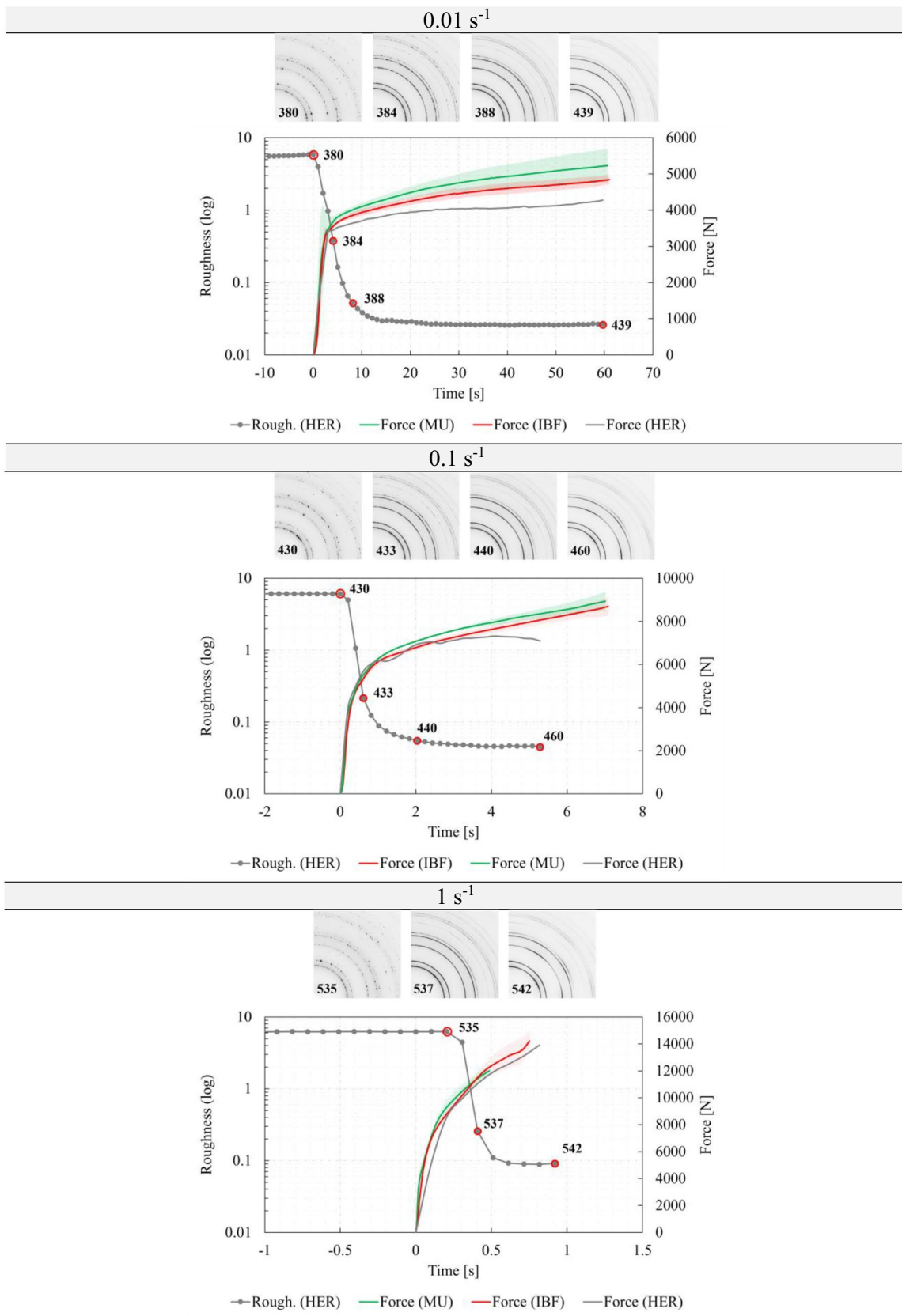


Fig. 30 Roughness of the (311) diffraction ring for uniaxial compression tests at 0.01 s^{-1} , 0.1 s^{-1} and 1 s^{-1} . Quarters of diffraction images are shown that are identified by their sequence numbers

The roughness clearly indicates the progress of the recrystallization process. When the roughness reaches the low plateau value, recrystallization has formed a new microstructure with a much smaller mean grain size. It should be noted that in the given diffraction geometry, a further reduction in grain size does not have an influence on the diffraction rings once they are homogeneous. The sensitivity on grain size can be influenced by the choice of the size of the gauge volume; a smaller gauge volume leads to spotty rings for smaller grain sizes.

Figure 31 presents together the flow stress and roughness evolution at the three tested strain rates. The results align with the literature, showing higher critical strain values for the initiation of DRX as the strain rate increases.

The *in-situ* results presented in this section are of significant scientific interest, demonstrating the effectiveness of *in-situ* testing for a better understanding of microstructural evolution in metallic materials under high-temperature testing conditions, illustrating the dynamics of the microstructural process, which is typically only analysed after finishing the test. In this regard, these experiments clearly indicate the relevant time frame for in-depth analyses of the microstructure state during thermomechanical processing. Another promising approach regarding *in-situ* measurements of mean grain size evolution at high temperature lies in the use of laser ultrasonic type techniques [47].

Conclusions

After having presented and discussed the results obtained in this extensive benchmark study, the main conclusions are outlined in this section. It is important to highlight that the experimental tests performed for this study were conducted with meticulous attention to detail, aiming to independently analyse the various factors affecting

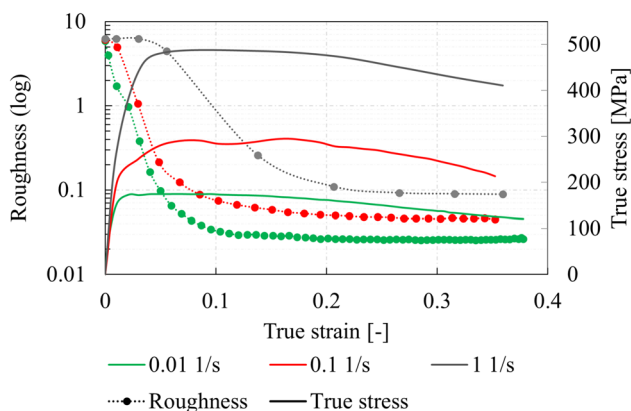


Fig. 31 Experimental *in-situ* roughness and flow stress curves under the three tested strain rates

both microstructural evolution and thermomechanical behaviour of metallic materials under high-temperature deformations. This approach was followed to ensure the most robust and objective conclusions in this challenging but crucial field of experimental mechanics in material science.

It is important to emphasize that this study was not intended to rank the testing machines in terms of their efficacy for material characterization but to provide an objective analysis of each aspect influencing the final experimental results.

The conclusions are organized into five main sections: grain growth, thermomechanical behaviour, dynamic recrystallization, virtual twins of experimental tests and *in-situ* analysis of microstructural evolution.

Grain growth

- The type of heating technology significantly impacts the grain growth evolution, with Joule heating promoting the fastest grain growth kinetics, followed by induction heating, and finally electrical resistance furnace heating, which exhibits the slowest grain growth kinetics.
- The higher the holding time, the bigger the differences observed on the resulting average grain size. The microstructure obtained with a heat treatment of 2 h at 1,150°C resulted in an average grain size more than twice as big when using Joule heating compared to the same heat treatment conducted in an electrical radiative furnace.
- The fact that the heating technology affects the grain growth evolution is evident, which is consistent with similar investigations found in the literature.

Thermomechanical behaviour

- Despite the compression tests being conducted under identical nominal conditions—temperature (1050°C) and macroscopic true strain rate (0.01 s⁻¹, 0.1 s⁻¹ and 1 s⁻¹)—and each machine demonstrated excellent repeatability with logical strain rate dependency when considered independently, significant scatter was observed in the flow curves obtained from the compression tests performed in the different facilities.
- The temperature homogeneity of the sample and the friction at the sample/tool interphase are likely the most influential factors on the differences observed on the flow curves, with the thermal gradient apparently having the greatest impact.
- The thermal gradient from the centre to the edges of the sample was higher in the dilatometers with induction heating (≈100 °C), followed by Gleeble machines with Joule heating (< 50 °C). Conventional thermomechanical machines equipped with electrical resistance furnaces

produce minimal thermal gradients, as the tools and the atmosphere are at the same temperature.

- Monitoring the sample temperature during heating and compression phases using multiple thermocouples is strongly recommended. If incorporating thermocouples complicates the experimental setup, preliminary tests should be conducted to empirically evaluate the thermal state of the sample, at least just before the compression takes place.
- Whether the macroscopic true strain rate is kept constant or the test is conducted at constant speed does not appear to significantly influence the flow behaviour of the tested material, at least if the initial speed is equal in both cases. However, using a constant macroscopic strain rate with a variable anvil speed is preferable, as it facilitates obtaining more comparable results with other equivalent tests and reduces equivalent strain rate variation at the sample centre, which is especially crucial for accurately assessing microstructural evolution.
- The influence of the stiffness of the facility and the eccentricity of the tools during compression was not analysed. Deformation dilatometers and Gleeble machines use high-temperature extensometers to eliminate the effect of the elastic deformation of the structure, while the conventional thermomechanical machines used in this study lacked this tool. Additionally, some samples exhibited slightly asymmetric deformations possibly due to the eccentricity of the tools, especially at high load conditions. The elastic deformation the machine suffers during compression and the tool eccentricity might have affected the flow curves. However, this effect was not quantitatively assessed.
- The smallest sample dimensions ($\text{Ø}5\text{mm} \times \text{L}10\text{mm}$) were used in the induction-heated dilatometers, which also exhibited the highest thermal gradients and friction values. These factors would typically result in higher flow stress values. However, the flow curves from the dilatometer tests are similar to those obtained at CEMEF, where the samples were thermally homogeneous. This unexpected similarity remains unexplained.
- Larger sample dimensions were employed in the Gleeble machines and conventional thermomechanical machines ($\text{Ø}10\text{mm} \times \text{L}12\text{mm}$ and $\text{Ø}10\text{mm} \times \text{L}15\text{mm}$, respectively) and, in general, showed less pronounced thermal gradients and friction values. Despite this, the flow curves from the Gleeble tests generally show lower stress values compared to those obtained from the conventional machine equipped with a resistance furnace at CEMEF. This variation in material behaviour is not yet fully understood.
- Attributing the differences observed in flow stress directly to the employed heating technology (furnace,

induction, or Joule heating) is challenging. Instead, the temperature gradient induced by each heating method seems to be more influential than the technology itself. However, the possibility that Joule heating could result in lower flow stresses cannot be completely ruled out, and it remains as an open question for further investigation.

- In general, to accurately characterise the thermomechanical behaviour of materials:
 - 1) The heating technology should be optimised to minimise thermal gradients, regardless of the employed heating method.
 - 2) Constant macroscopic true strain rate is recommended for tool kinematics.
 - 3) Friction should be reduced by using appropriate lubrication.
 - 4) Homogeneous and symmetrical sample deformations should be guaranteed.
- If friction in the tool/sample interface and the sample thermal gradient are significant and cannot be further minimised, inverse simulation is highly recommended to accurately calibrate material thermomechanical models of the tested material. To achieve this, it is essential to employ precise experimental thermal, frictional, and kinematic boundary conditions.

Dynamic recrystallization

- Despite the fact that the tests being conducted under the same nominal temperature and strain rate conditions, significant scatter was observed in the DRX results, with notable differences in both the recrystallized fraction and recrystallized grain size.
- The selected zone in the central area of the sample for EBSD analysis is not considered to be the cause of the observed differences. An EBSD location and magnification influence analysis was conducted on a sample tested in the dilatometer, which was the smallest and hence the most critical sample. The selected zone was found to have a minor impact on the resulting average recrystallized grain size, and although higher differences were observed in the DRX fraction, these do not appear to account for the significant scatter in the DRX results.
- Friction significantly influences the equivalent strain at the centre of the sample, where EBSD analyses are typically conducted, leading to higher strain gradients with increased friction. Therefore, minimizing friction is beneficial for reducing the strain gradients and diminishing microstructural evolution gradients across the cross-section of the sample.

- Temperature difference is not considered the main cause of variation in the DRX results. The temperature at the centre of the sample, where the DRX analysis was conducted, was monitored in both the dilatometers and Gleeble machines. Temperature measurements in these facilities were closely aligned with the nominal temperature. In conventional machines equipped with electrical furnaces, the initial temperature was verified at AFRC using a thermocouple attached to the sample centre. At CEMEF, sufficient heating time was likely used to ensure that the testing temperature was reached, at least at the sample centre.
- The quenching time was comparable across all the cases (< 2 s), except for AFRC, where samples were quenched in a longer time (≈ 15 s). Consequently, the larger average grain sizes and higher recrystallized fractions observed at AFRC are attributed to the extended quenching time, which results in a significant post-dynamic evolution. In contrast, variations in quenching time in the rest of the facilities are not considered the primary reason for the observed variations. Rapid post-forming quenching (< 2 s) is essential for accurately characterising the DRX phenomenon.
- The DRX results obtained from tests conducted in both the dilatometers and the furnace-heated conventional machine at CEMEF are generally comparable. However, Gleeble results indicate larger grain sizes and faster DRX kinetics (higher recrystallized fractions), especially at lower strain rates (0.01 s^{-1} and 0.1 s^{-1}). At the highest tested strain rate (1 s^{-1}), the results from the Gleeble tests are more consistent with those from the other facilities.
- Based on the obtained results, it is probable that the heating technology influences DRX evolution, with Joule heating having the most significant impact, especially at lower strain rates. This conclusion is supported by the grain growth results, which show that Joule heating clearly accelerates grain growth, and by the Gleeble results, where lower strain rates correspond with faster DRX kinetics and larger recrystallized grain sizes compared to those obtained from the tests in the dilatometers and the CEMEF conventional machine.
- When using laboratory tests to reproduce a part of an industrial process, e.g. to identify material-dependent model parameters, a particular attention should be paid to the heating technology especially when investigating microstructural evolutions.

Virtual twin of experimental tests

- Virtual twins of uniaxial compression tests were developed using the FORGE® simulation software to estimate the thermomechanical path (equivalent strain and strain rate) experienced at the sample centre, where EBSD

analyses were conducted. The final equivalent strain at the sample centre is a critical parameter for the correct evaluation of the DRX kinetics.

- Various simulation strategies were evaluated, and based on the results, the centre strains were calculated using an isothermal model. It was demonstrated that the strain field at the sample centre is primarily influenced by the barrelling shape, which is mainly affected by friction. Additionally, the numerical model could be adapted for each testing setup and condition by adjusting the friction coefficient. Therefore, this approach effectively corrects for both friction effects and temperature inhomogeneities using a single parameter and a simple numerical model that does not account for heat transfer.
- It is important to mention that to develop a representative simulation model, it is essential to acquire accurate experimental measurements, including the final sample geometry for friction estimation, temperature conditions, and tool kinematics.

In-situ microstructural evolution analysis

- Although no quantitative GG and DRX results were obtained in this study, the *in-situ* testing demonstrated significant potential for characterizing and understanding microstructural evolution phenomena during high-temperature testing. The analysis of diffraction ring roughness was employed to assess grain size evolution, which showed consistent results in both GG and DRX tests.
- The GG heat treatments revealed a pronounced growth rate during the initial 3 min, followed by a plateau phase. This plateau indicates a deceleration in the growth rate rather than a cessation of GG, as evidenced by the GG tests conducted in the other facilities. Although quantitative measurements of the final average grain size were not calculated, the *in-situ* testing provided valuable qualitative results to understand the kinetics of GG.
- Regarding the *in-situ* DRX analysis, although quantitative results on recrystallized grain size and fraction were not obtained, the evolution of DRX was clearly observed through changes in the roughness of the diffraction rings. Interestingly, the strain rate dependency of DRX was clearly seen, with higher critical DRX strains observed at increased strain rates, consistent with existing literature. *In-situ* testing proved to be a powerful tool, offering valuable experimental results of key DRX parameters, such as the critical strain at which DRX is triggered.

Acknowledgements The authors would like to thank the ESAFORM European Scientific Association for Material Forming for funding this research through the Benchmark Grant. It has been a great pleasure to collaborate on such a significant and impactful topic, which holds

importance not only for the scientific community but also for the industry. The collective effort of all involved institutions has been invaluable to the success of this benchmark study.

At Mondragon University, authors acknowledge the support provided by the Basque Government and ULMA Forged Solutions through the OGFORGE project (ZL-2018/00462, ZL-2019/00161), as well as Tubacex for their support by PROMAX and ALYMICRO (KK-2019/00041) projects. The work carried out at CEMEF has been funded by the French ANR industrial Chairs DIGIMU (Grant No. ANR-16-CHIN-0001) and RealIMotion (Grant No. ANR-22-CHIN-0003). The authors from LFT would like to extend special thanks to Martin Kraus for his invaluable contributions and support in realising the institute's participation in this benchmark.

At AGH University of Krakow, Łukasz Madej acknowledges financial assistance from the National Science Centre Poland (Project No. 2019/35/B/ST8/00046). Both Łukasz Madej and Kamil Muszka would also like to acknowledge the research support received through the "Excellence initiative—research university" program at AGH University of Krakow.

Finally, authors would like to express their gratitude to DESY (Hamburg, Germany), a member of the Helmholtz Association HGF, for providing experimental facilities at PETRA III at DESY, specifically on the P07 beamline.

Data availability Open access database is available in the Zenodo repository: <https://doi.org/10.5281/zenodo.13917402>.

Declarations

Conflict of interest The authors declare that they have no conflict of interest.

Open Access This article is licensed under a Creative Commons Attribution-NonCommercial-NoDerivatives 4.0 International License, which permits any non-commercial use, sharing, distribution and reproduction in any medium or format, as long as you give appropriate credit to the original author(s) and the source, provide a link to the Creative Commons licence, and indicate if you modified the licensed material. You do not have permission under this licence to share adapted material derived from this article or parts of it. The images or other third party material in this article are included in the article's Creative Commons licence, unless indicated otherwise in a credit line to the material. If material is not included in the article's Creative Commons licence and your intended use is not permitted by statutory regulation or exceeds the permitted use, you will need to obtain permission directly from the copyright holder. To view a copy of this licence, visit <http://creativecommons.org/licenses/by-nc-nd/4.0/>.


References

- Altan T, Ngaile G, Shen G (2005) Cold and Hot Forging: Fundamentals and Applications. <https://doi.org/10.1361/chff2005p001>
- Prasad YVRK, Rao KP, Sasidhara S (2015) Hot Working Guide - A Compendium of Processing Maps. 2nd ed. 10.1016/B978-0-08-033454-7.50019-X
- Doherty RD, Hughes DA, Humphreys FJ, Jonas JJ, Juul Jensen D, Kassner ME et al (1997) Current issues in recrystallization: a review. *Mater Sci Eng A* 238:219–274. [https://doi.org/10.1016/S0921-5093\(97\)00424-3](https://doi.org/10.1016/S0921-5093(97)00424-3)
- Semiatin SL (2005) ASM Handbook: Metalworking: Bulk Forming. vol. 14A. doi: 10.1361/asmhba0003971
- Dieter GE, Kuhn HA, Semiatin SL (2023) Handbook of workability and process design. <https://doi.org/10.1361/hwpd2003p232>
- Rollett A, Humphreys F, Rohrer GS, Hatherly M (2004) Recrystallization and Related Annealing Phenomena - Chapter 5 - The Mobility and Migration of Boundaries. <https://doi.org/10.1016/B978-008044164-1/50009-8>
- Rollett A, Humphreys F, Rohrer GS, Hatherly M (2004) Recrystallization and Related Annealing Phenomena - Chapter 11 - Grain Growth Following Recrystallization. <https://doi.org/10.1016/B978-008044164-1/50015-3>
- Huang K, Logé RE (2016) A review on dynamic recrystallization phenomena in metallic materials. *Mater Des* 111:548–574. <https://doi.org/10.1016/j.matdes.2016.09.012>
- Sakai T, Belyakov A, Kaibyshev R, Miura H, Jonas JJ (2014) Dynamic and post-dynamic recrystallization under hot, cold and severe plastic deformation conditions. *Prog Mater Sci* 60:130–207. <https://doi.org/10.1016/j.pmatsci.2013.09.002>
- Davis JR (2000) ASM Specialty Handbook - Nickel, Cobalt, and Their Alloys. <https://doi.org/10.1361/ncta2000p013>
- Freund L, Langlois L, Bigot R, Gyss O (2020) Study of the dynamic recrystallization of Inconel 625 alloys through cogging. *Procedia Manuf* 50:658–662. <https://doi.org/10.1016/j.promfg.2020.08.118>
- Tehovnik F, Burja J, Podgornik B, Godec M, Vode F (2015) Microstructural evolution of Inconel 625 during hot rolling. *Mater Technol* 49:801–806. <https://doi.org/10.17222/mit.2015.274>
- Shengli G, Defu L, Qingmiao G, Zhigang W, Haijian P, Jie H (2012) Investigation on hot workability characteristics of Inconel 625 superalloy using processing maps. *J Mater Sci* 47:5867–5878. <https://doi.org/10.1007/s10853-012-6488-x>
- Qingmiao G, Defu L, Shengli G, Haijian P, Jie H (2011) The effect of deformation temperature on the microstructure evolution of Inconel 625 superalloy. *J Nucl Mater* 414:440–450. <https://doi.org/10.1016/j.jnucmat.2011.05.029>
- Nicolaÿ A, Fiorucci G, Franchet JM, Cormier J, Bozzolo N (2019) Influence of strain rate on subsolvus dynamic and post-dynamic recrystallization kinetics of Inconel 718. *Acta Mater* 174:406–417. <https://doi.org/10.1016/j.actamat.2019.05.061>
- Kumar SSS, Raghu T, Bhattacharjee PP, Rao GA, Borah U (2017) Work hardening characteristics and microstructural evolution during hot deformation of a nickel superalloy at moderate strain rates. *J Alloys Compd* 709:394–409. <https://doi.org/10.1016/j.jallcom.2017.03.158>
- Uranga P, Gutiérrez I, López B (2013) Determination of recrystallization kinetics from plane strain compression tests. *Mater Sci Eng A* 578:174–180. <https://doi.org/10.1016/j.msea.2013.04.077>
- Maire L, Scholtes B, Moussa C, Bozzolo N, Muñoz DP, Settefrati A et al (2017) Modeling of dynamic and post-dynamic recrystallization by coupling a full field approach to phenomenological laws. *Mater Des*. <https://doi.org/10.1016/j.matdes.2017.08.015>
- Stefani N, Bylya O, Reshetov A, Blackwell P (2017) On the applicability of JMAK-type models in predicting IN718 microstructural evolution. *Comput Methods Mater Sci* 17:59–68
- Bernacki M, Bozzolo N, de Micheli P, Flipon B, Fausty J, Maire L, Florez S (2019) Numerical modeling of recrystallization in a level set finite element framework for application to industrial processes. *Recrystallization: Types, Techniques and Applications*
- Madej L (2017) Digital/virtual microstructures in application to metals engineering – A review. *Arch Civ Mech Eng* 17:839–854. <https://doi.org/10.1016/j.acme.2017.03.002>
- Zouari M, Bozzolo N, Loge RE (2016) Mean field modelling of dynamic and post-dynamic recrystallization during hot deformation of Inconel 718 in the absence of δ phase particles. *Mater Sci Eng A* 655:408–424. <https://doi.org/10.1016/j.msea.2015.12.102>

23. Stockinger M, Tockner J (2005) Optimizing the forging of critical aircraft parts by the use of finite element coupled microstructure modeling. Proc Int Symp Superalloys Var Deriv 87–95. https://doi.org/10.7449/2005/superalloys_2005_87_95
24. De Micheli P, Settefrati A, Marie S, Barlier J, Lasne P, Scholtes B et al (2015) Towards the simulation of the whole manufacturing chain processes with FORGE. Proc Int Conf 'New Dev Forg Technol. pp 1–25
25. Agirre J, Abedul D, Saenz de Argandoña E, Otegi N, Galdos L, Erice B (2023) An automatic thermo-mechanical testing apparatus for metal forming applications. Int J Impact Eng 182:104764. [10.1016/j.ijimpeng.2023.104764](https://doi.org/10.1016/j.ijimpeng.2023.104764)
26. Fritton M, Kümmel F, Kirchmayer A, Stark A, Hafez Haghghat M, Gehrman B et al (2023) Investigation of the hot deformation behavior in VDM® Alloy 780 by In Situ High-Energy X-Ray Diffraction. Metall Mater Trans A Phys Metall Mater Sci 54:2037–2051. <https://doi.org/10.1007/s11661-022-06942-5>
27. Guo Q, Li D, Peng H, Guo S, Hu J, Du P (2012) Nucleation mechanisms of dynamic recrystallization in Inconel 625 superalloy deformed with different strain rates. Rare Met 31:215–220. <https://doi.org/10.1007/s12598-012-0494-7>
28. Nicolaj A, Franchet JM, Cormier J, Logé RE, Fiorucci G, Fausty J et al (2021) Influence of Joule Effect Heating on Recrystallization Phenomena in Inconel 718. Metall Mater Trans A Phys Metall Mater Sci 52:4572–4596. <https://doi.org/10.1007/s11661-021-06411-5>
29. Rheinheimer W, Parras JP, Preusker JH, De Souza RA, Hoffmann MJ (2019) Grain growth in strontium titanate in electric fields: The impact of space-charge on the grain-boundary mobility. J Am Ceram Soc 102:3779–3790. <https://doi.org/10.1111/jace.16217>
30. Flipon B, Grand V, Murgas B, Gaillac A, Nicolaj A, Bozzolo N et al (2021) Grain size characterization in metallic alloys using different microscopy and post-processing techniques. Mater Charact 174:110977. <https://doi.org/10.1016/j.matchar.2021.110977>
31. Wright SI (2010) A Parametric Study of Electron Backscatter Diffraction based Grain Size Measurements. Pract Metallogr 47:16–33. <https://doi.org/10.3139/147.110060>
32. ASTM (2013) E112 - Standard Test Methods for Determining Average Grain Size. <https://doi.org/10.1520/E0112-12>
33. Schwartz AJ, Kumar M, Adams BL, Field DP. Electron backscatter diffraction in materials science. Electron Backscatter Diffr Mater Sci 2009:1–403. <https://doi.org/10.1007/978-0-387-88136-2>.
34. Febrari A, Gelfi M, Giovanardi R, Montesano L, Pola A, Montani R et al (2019) Corrosion and mechanical properties of age-hardened UNS N06625 forged bars for oil and gas applications. Mater Corros 70:1755–1763. <https://doi.org/10.1002/maco.201910856>
35. Agirre J (2022) Development of a thermomechanical tester for intermediate strain rates and phenomenological modelling of microstructural evolution: application to hot forging of Inconel 625.
36. Zhang C, Zhang L, Shen W, Xu Q, Cui Y (2017) The processing map and microstructure evolution of Ni-Cr-Mo-based C276 superalloy during hot compression. J Alloys Compd 728:1269–1278. <https://doi.org/10.1016/j.jallcom.2017.09.107>
37. Guest RP, Tin S (2005) The Dynamic and Metadynamic Recrystallisation of IN 718. Superalloys 718, 625, 706. Var Deriv 1:373–383. https://doi.org/10.7449/2005/Superalloys_2005_373_383
38. Hammersley A. FIT2D n.d. <https://www.esrf.fr/computing/scientific/FIT2D/>
39. Hammersley AP, Svensson SO, Hanfland M, Fitch AN, Häusermann D (1996) Two-dimensional detector software: From real detector to idealised image or two-theta scan. High Press Res 14:235–248. <https://doi.org/10.1080/08957959608201408>
40. Freund LP, Stark A, Pyczak F, Schell N, Göken M, Neumeier S (2018) The grain boundary pinning effect of the μ phase in an advanced polycrystalline γ/γ' Co-base superalloy. J Alloys Compd 753:333–342. <https://doi.org/10.1016/j.jallcom.2018.04.204>
41. Shotri R, Ogura T, Geng P, Morisada Y, Ushioda K, Fujii H (2023) Numerical and experimental investigation of pressure-controlled joule-heat forge welding of steel tubes. J Manuf Process 106:240–253. <https://doi.org/10.1016/j.jmappro.2023.10.007>
42. Fomin A, Koshuro V, Shchelkunov A, Aman A, Fomina M, Kalganova S (2021) Simulation and experimental study of induction heat treatment of titanium disks. Int J Heat Mass Transf 165:120668. <https://doi.org/10.1016/j.ijheatmasstransfer.2020.120668>
43. Hielscher R. MTEX Matlab Toolbox n.d. <https://mtebox.github.io/>.
44. Bachmann F, Hielscher R, Jupp PE, Pantleon W, Schaeben H, Wegert E (2010) Inferential statistics of electron backscatter diffraction data from within individual crystalline grains. J Appl Crystallogr 43:1338–1355. <https://doi.org/10.1107/S002188981003027X>
45. Burke JE, Turnbull D. Recrystallization and grain growth. Prog Met Phys 1952;3. [https://doi.org/10.1016/0502-8205\(52\)90009-9](https://doi.org/10.1016/0502-8205(52)90009-9).
46. Zhang S, Wang J, Huang L, Srivatsa S, Zhou K, Huang Z et al (2021) Correction of flow stress data due to non-homogeneous deformation and thermal conditions during hot compression testing of a polycrystalline nickel-base superalloy. J Mater Sci 56:7727–7739. <https://doi.org/10.1007/s10853-020-05714-z>
47. Garcin T, Schmitt JH, Militzer M (2016) *In-situ* laser ultrasonic grain size measurement in superalloy INCONEL 718. J Alloys Compd 670:329–336. <https://doi.org/10.1016/j.jallcom.2016.01.222>

Publisher's Note Springer Nature remains neutral with regard to jurisdictional claims in published maps and institutional affiliations.

Authors and Affiliations

Julen Agirre¹  · Daniel Bernal¹ · Baptiste Flipon² · Marc Bernacki² · Holger Brüggemann³ · David Bailly³ · Marion Merklein⁴ · Hinnerk Hagenah⁴ · Jan Henning Risse⁴ · Łukasz Madej⁵ · Krzysztof Muszka⁵ · Kamil Cichocki⁵ · Łukasz Poloczek⁶ · Olga Bylya⁷ · Aleksey Reshetov⁷ · Pascal De Micheli⁸ · Julien Barlier⁸ · Andreas Stark⁹ · Uceu F. H. Suhuddin¹⁰ · Peter Staron⁹ · Benjamin Klusemann^{10,11} · Lander Galdos¹

✉ Julen Agirre
jagirreb@mondragon.edu
Lander Galdos
lgaldos@mondragon.edu

¹ Mechanics and Industrial Production Department, Mondragon Unibertsitatea, Loramendi 4, 20500 Mondragon, Spain

² Mines Paris - PSL, CNRS, CEMEF, UMR 7635, 06904 Sophia Antipolis, France

³ Institute of Metal Forming (IBF), RWTH Aachen University, Intzestr. 10, 52072 Aachen, Germany

⁴ Institute of Manufacturing Technology, Friedrich-Alexander Universität Erlangen-Nürnberg, Egerlandstr. 13, 91058 Erlangen, Germany

⁵ AGH University of Krakow, 30 Mickiewicza Ave, 30-059 Kraków, Poland

⁶ Materials Research Group, Lukaszewicz Research Network, Upper Silesian Institute of Technology, Karola Miarki 12-14, 44-100 Gliwice, Poland

⁷ National Manufacturing Institute of Scotland, University of Strathclyde, 3 Netherton Sq, Paisley, Renfrew PA3 2EF, UK

⁸ Transvalor SA, 950 Avenue Roumanille - CS 40237, 06904 Sophia Antipolis Cedex Biot, France

⁹ Institute of Materials Physics, Helmholtz-Zentrum Hereon, Max-Planck-Str. 1, 21502 Geesthacht, Germany

¹⁰ Institute of Material and Process Design, Helmholtz-Zentrum Hereon, Max-Planck-Str. 1, 21502 Geesthacht, Germany

¹¹ Institute for Production Technology and Systems, Leuphana University Lüneburg, Universitätsallee 1, 21335 Lüneburg, Germany